Inorganic Chemistry

Article

pubs.acs.org/IC

Pentafluoro-oxotellurate(VI) Anions of Mercury(II); Syntheses and Structures of $[Hg(OTeF_5)_4]^{2-}$, $[Hg(OTeF_5)_5]^{3-}$, $[Hg_2(OTeF_5)_6]^{2-}$, $[Hg(OTeF_5)_4]^{2-}\cdot Hg(OTeF_5)_2$, and $[Hg_2(OTeF_5)_7]^{3-}\cdot Hg(OTeF_5)_2$

John R. DeBackere, Hélène P. A. Mercier, and Gary J. Schrobilgen*

Department of Chemistry, McMaster University, Hamilton, Ontario L8S 4M1, Canada

Supporting Information

ABSTRACT: Mercury(II) anions derived from the F_5TeO- (teflate) group were synthesized and structurally characterized. The salts, $[N(CH_2CH_3)_4]_2[Hg(OTeF_5)_4]$, $[N(CH_3)_4]_3[Hg(OTeF_5)_5]$, $[N(CH_2CH_3)_4]_3[Hg(OTeF_5)_5]$, $[N(CH_3)_4]_2[Hg_2(OTeF_5)_6]$, $Cs_2[Hg(OTeF_5)_4]\cdot Hg(OTeF_5)_2$, and $\{Cs_3[Hg_2(OTeF_5)_7]\cdot Hg(OTeF_5)_2\}\cdot 4SO_2ClF$, were obtained by reaction of $Hg(OTeF_5)_2$ with $[M][OTeF_5]$ ($M = [N(CH_3)_4]^+$, $[N(CH_2CH_3)_4]^+$, Cs^+) and were characterized by low-temperature single-crystal X-ray diffraction and low-temperature Raman spectroscopy. Unlike in the extensively fluorine-bridged solid-state structures of $[HgF_3]^-$ and $[HgF_4]^{2-}$, the less basic and more sterically demanding teflate ligands of the Hg(II) anions show less tendency to bridge. The anions exhibit a variety of structural motifs, ranging from well-isolated tetrahedral $[Hg(OTeF_5)_4]^{2-}$ and square-pyramidal $[Hg(OTeF_5)_5]^{3-}$ to the chain structures, $[Hg_2(OTeF_5)_6]^{2-}$ and $[Hg_2(OTeF_5)_7]^{3-}\cdot Hg(OTeF_5)_2$. The geometrical parameters and vibrational frequencies of $[Hg(OTeF_5)_4]^{2-}$ (S_4), $[Hg(OTeF_5)_5]^{3-}$ (C_1), and $[Hg_2(OTeF_5)_6]^{2-}$ (D_2) anions, as well as the hypothetical $[Hg_3(OTeF_5)_8]^{2-}$ (C_1) anion, were calculated using density functional theory methods (PBE1PBE/def2-TZVPP), which aided in the assignment of the Raman spectra of $[Hg(OTeF_5)_4]^{2-}$, $[Hg(OTeF_5)_5]^{3-}$, $[Hg_2(OTeF_5)_6]^{2-}$, and $Cs_2[Hg(OTeF_5)_4]\cdot Hg(OTeF_5)_2$. The calculated geometries were used to assess the effects of solid-state interionic interactions on the anion geometries. For the most part, the gross gas-phase trigonal bipyramidal (tbp) geometry of $[Hg(OTeF_5)_5]^{3-}$ adheres to the predicted VSEPR geometry but contrasts with the solid-state anion structures, which have square-pyramidal geometries or geometries that lie between square pyramidal- and tbp-geometries. However, the bond length order calculated for the Hg−O bonds of tbp-$[Hg(OTeF_5)_5]^{3-}$, $Hg-O_{eq} > Hg-O_{ax}$, is opposite to that predicted by the VSEPR model of molecular geometry. Natural bond orbital analyses provided the associated Mayer bond orders, Mayer valencies, and natural population analysis charges.

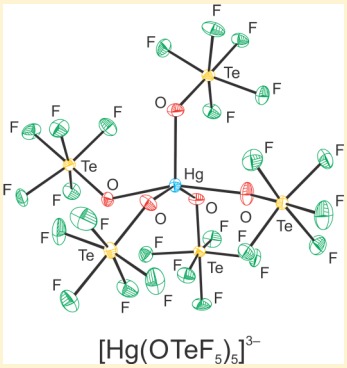

INTRODUCTION

Mercury(II) halogeno-anions have been extensively studied, revealing a considerable structural diversity in the solid state. From the large number of chloro-, bromo-, and iodomercury(II) anions that have been synthesized and structurally characterized by single-crystal X-ray diffraction, it is evident that the solid-state anion structures often do not reflect the empirical formula.[1] For example, over 30 chloromercury(II) anions have been reported with structures ranging from isolated mononuclear $[HgCl_3]^-$ and dinuclear $[Hg_2Cl_6]^{2-}$ to infinite chain $[HgCl_3^-]_\infty$ anions.[1] The mononuclear halogenomercury(II) anions, $[HgX_3]^-$ (X = Cl,[1] I[2]) and $[HgX_4]^{2-}$ (X = Cl,[1] Br,[3] I[4]), are well-known, but examples of $[HgX_5]^{3-}$ and $[HgX_6]^{4-}$ are limited to the trigonal bipyramidal anions of $[Cr(NH_3)_6][HgCl_5]$,[5] $[Co(NH_3)_6][HgBr_5]$,[6] and $[H_3N(CH_2)_2NH_2(CH_2)_2NH_3]_2[HgCl_5]$[7] and the octahedral anions of $[Tl_4][HgX_6]$ (X = Br,[8] I[9]) and $[NH_4]_4[HgBr_6]$.[10] Halogen-bridging between mercury(II) atoms results in the formation of polynuclear anions. Among those that have been structurally characterized are the halogen-bridged dinuclear $[Hg_2X_6]^{2-}$ and $[Hg_2X_7]^{3-}$ (X = Cl,[1] I[11,12]) anions; trinuclear $[Hg_3Cl_7]^{-1}$ and $[Hg_3X_8]^{2-}$ (X = Cl,[1] I[13]) anions; higher polynuclear anions such as $[Hg_4Cl_{14}]^{6-}$, $[Hg_5Cl_{11}]^-$, and $[Hg_6Cl_{13}]^-$; and examples of extensively halogen-bridged polymeric and network structures.[1] Although not comprehensive, these examples illustrate the considerable structural diversity that exists among the heavier halogenomercury(II) anions. In the case of fluoromercury(II) anions, the greater propensity for fluorine to bridge has limited the number of structurally characterized examples to the extended three-dimensional network solids, $MHgF_3$ (M = K, Rb, Cs)[14] and M_2HgF_4 (M = Rb, Cs).[15] The geometries of the $[HgF_3]^-$ (D_{3h}) and $[HgF_4]^{2-}$ (T_d) anions have been calculated in the gas phase.[16]

The pentafluoro-orthotellurate group, F_5TeO- (teflate), is a bulky pseudohalide with a group electronegativity (3.88[17] and 3.87[18]) that is comparable to that of fluorine (3.98, Allred–Rochow scale). The binding strength of the teflate ligand has been shown to follow the order $Cl^- > [F_5TeO]^- > [ClO_4]^-$ for Fe(TPP)(L) ($[TPP]^{2-}$ = *meso*-tetraphenylporphinate and L = Cl^-, $[F_5TeO]^-$, $[ClO_4]^-$).[19] The F_5TeO- group is terminally bonded in the majority of its compounds, with only a few examples of μ−oxygen bonding. The latter bonding modality has been

Received: October 28, 2014
Published: January 21, 2015

DOI: 10.1021/ic502602p
Inorg. Chem. 2015, 54, 1606−1626

predominantly found in neutral metal compounds, e.g., $[TlOTeF_5(mes)_2]_2$·mes (mes = 1,3,5-trimethylbenzene),[20] $Au(OTeF_5)_3$,[21] $[AgOTeF_5(C_6H_5CH_3)_2]_2$,[22] $[AgOTeF_5(1,2\text{-}C_2H_4Cl_2)]_2$,[23] and $[Zn(OTeF_5)_2(C_6H_5NO_2)_2]_2$,[24] as well as in the salts $[Ag(CO)][B(OTeF_5)_4]$,[25] and $Ag(CH_2C1_2)Pd(OTeF_5)_4$.[26] Unlike HgF_2 (Hg coordination number = 8), which possesses an extended three-dimensional solid-state structure similar to $[HgF_3]^-$ and $[HgF_4]^{2-}$ (Hg coordination number = 6), the crystal structure of $Hg(OTeF_5)_2$ consists of discrete molecular units that only interact through long Hg---O and Hg---F intermolecular contacts.[27] Consequently, mercury teflate anions are not expected to form extensively teflate-bridged lattices. Considering the notable differences between the solid-state structures of HgF_2 and $Hg(OTeF_5)_2$, it was of interest to determine if teflate analogues of halogenomercury(II) anions could be formed and to establish their structural diversity.

Anions derived from the teflate group are known for their weakly coordinating properties and their ability to stabilize strong electrophiles and high oxidation states.[28] The $[M(OTeF_5)_n]^{m-}$ anions that have been characterized in the solid state are limited to the tetrahedral $[B(OTeF_5)_4]^-$,[29,30] square-planar $[I(OTeF_5)_4]^-$[31] and $[Pd(OTeF_5)_4]^{2-}$,[26] square-pyramidal $[Te(OTeF_5)_5]^-$,[32] and octahedral $[M(OTeF_5)_6]^-$ (M = As,[33] Sb,[32,34] Bi,[33] Nb,[34] Ta[34]) and $M(OTeF_5)_6^{2-}$ (M = Ti, Zr, Hf) anions.[34] Among the group 12 elements, three salts containing the $[Zn(OTeF_5)_4]^{2-}$ anion have been briefly mentioned in the literature.[35] The salt, $Ag_2[Zn(OTeF_5)_4]$, was characterized by infrared and ^{19}F NMR spectroscopy, whereas $[Ag(CO)]_2[Zn(OTeF_5)_4]$ and $[Ag(CO)_2]_2[Zn(OTeF_5)_4]$ were characterized by infrared and ^{13}C MAS NMR spectroscopy.[36]

The present study describes the syntheses of a series of Hg(II) teflate anions and their characterizations by low-temperature, single-crystal X-ray diffraction; Raman spectroscopy; and quantum-chemical calculations. The anion series represents the first examples of mercury(II) teflate anions that have been synthesized and structurally characterized.

RESULTS AND DISCUSSION

Syntheses. Low-temperature Raman spectra were recorded on colorless crystalline samples obtained by slow solvent evaporation at 0 °C unless otherwise stated. Single crystals suitable for X-ray structure determinations were obtained from the Raman samples. The compounds showed high solubilities in SO_2 and CH_2Cl_2, whereas SO_2ClF provided low to moderate solubilities.

(a) $[N(CH_2CH_3)_4]_2[Hg(OTeF_5)_4]$ and $[N(CH_2CH_3)_4]_3[Hg(OTeF_5)_5]$. The $[N(CH_2CH_3)_4]_2[Hg(OTeF_5)_4]$ salt was synthesized by the reaction of $Hg(OTeF_5)_2$ with $[N(CH_2CH_3)_4][OTeF_5]$ (ca. 1:2 molar ratio) in SO_2ClF solvent at room temperature (eq 1).

$$Hg(OTeF_5)_2 + 2[N(CH_2CH_3)_4][OTeF_5] \rightarrow [N(CH_2CH_3)_4]_2[Hg(OTeF_5)_4] \quad (1)$$

The salt, $[N(CH_2CH_3)_4]_3[Hg(OTeF_5)_5]$, was synthesized by combining $Hg(OTeF_5)_2$ with $[N(CH_2CH_3)_4][OTeF_5]$ (ca. 1:4 molar ratio) in SO_2ClF solvent at room temperature (eq 2).

$$Hg(OTeF_5)_2 + 3[N(CH_2CH_3)_4][OTeF_5] \rightarrow [N(CH_2CH_3)_4]_3[Hg(OTeF_5)_5] \quad (2)$$

(b) $[N(CH_3)_4]_3[Hg(OTeF_5)_5]$ and $[N(CH_3)_4]_2[Hg_2(OTeF_5)_6]$. The synthesis of $[N(CH_3)_4]_3[Hg(OTeF_5)_5]$ was carried out in liquid SO_2 by combining a stoichiometric excess of $[N(CH_3)_4][OTeF_5]$ with $Hg(OTeF_5)_2$ (2.2:1 molar ratio) at 0 °C (eq 3).

$$Hg(OTeF_5)_2 + 3[N(CH_3)_4][OTeF_5] \rightarrow [N(CH_3)_4]_3[Hg(OTeF_5)_5] \quad (3)$$

The salt, $[N(CH_3)_4]_2[Hg_2(OTeF_5)_6]$, was synthesized at room temperature by the reaction of $Hg(OTeF_5)_2$ with $[N(CH_3)_4][OTeF_5]$ in a 1:1 molar ratio using CH_2Cl_2 as the solvent (eq 4).

$$2Hg(OTeF_5)_2 + 2[N(CH_3)_4][OTeF_5] \rightarrow [N(CH_3)_4]_2[Hg_2(OTeF_5)_6] \quad (4)$$

(c) $Cs_2[Hg(OTeF_5)_4]\cdot Hg(OTeF_5)_2$ and $\{Cs_3[Hg_2(OTeF_5)_7]\cdot Hg(OTeF_5)_2\}\cdot 4SO_2ClF$. The reaction of $Hg(OTeF_5)_2$ with a stoichiometric excess of $Cs[OTeF_5]$ (ca. 1:4 molar ratio) in SO_2ClF solvent at room temperature resulted in the formation of $Cs_2[Hg(OTeF_5)_4]\cdot Hg(OTeF_5)_2$ according to eq 5.

$$2Hg(OTeF_5)_2 + 2Cs[OTeF_5] \rightarrow Cs_2[Hg(OTeF_5)_4]\cdot Hg(OTeF_5)_2 \quad (5)$$

At a 1:2 molar ratio of $Hg(OTeF_5)_2$:$Cs[OTeF_5]$, crystalline $\{Cs_3[Hg_2(OTeF_5)_7]\cdot Hg(OTeF_5)_2\}\cdot 4SO_2ClF$ was obtained from SO_2ClF and characterized by single-crystal X-ray diffraction. Regardless of the stoichiometric excess of $Cs[OTeF_5]$ that was used, no other species were isolated or identified by Raman spectroscopy.

(d) Attempted Syntheses of $[N(CH_2CH_3)_4][Hg(OTeF_5)_3]$ and $[N(CH_2CH_3)_4]_4[Hg(OTeF_5)_6]$. Reactions employing high molar ratios of $[N(CH_2CH_3)_4][OTeF_5]$ to $Hg(OTeF_5)_2$ only resulted in $[N(CH_2CH_3)_4]_2[Hg(OTeF_5)_4]$ and $[N(CH_2CH_3)_4]_3[Hg(OTeF_5)_5]$. Attempts to synthesize the mononuclear $[Hg(OTeF_5)_3]^-$ anion using a 1:1 molar ratio of $[N(CH_2CH_3)_4][OTeF_5]$ to $Hg(OTeF_5)_2$ resulted in a colorless vitreous solid that failed to diffract in a X-ray beam. The Raman spectrum of the material showed bands similar to those identified for the anion of $[N(CH_3)_4]_2[Hg_2(OTeF_5)_6]$, suggesting that the $[N(CH_2CH_3)_4]^+$ salt of $[Hg_2(OTeF_5)_6]^{2-}$ had been synthesized.

X-ray Crystallography. Details of the data collection parameters and other crystallographic information for $[N(CH_2CH_3)_4]_2[Hg(OTeF_5)_4]$, $[N(CH_3)_4]_3[Hg(OTeF_5)_5]$, $[N(CH_2CH_3)_4]_3[Hg(OTeF_5)_5]$, $[N(CH_3)_4]_2[Hg_2(OTeF_5)_6]$, $Cs_2[Hg(OTeF_5)_4]\cdot Hg(OTeF_5)_2$, and $\{Cs_3[Hg_2(OTeF_5)_7]\cdot Hg(OTeF_5)_2\}\cdot 4SO_2ClF$ are provided in Table 1. Selected bond lengths and angles for the title anions are listed in Tables 2−6, and a full list of their geometrical parameters along with the structural parameters of the $[N(CH_3)_4]^+$ and $[N(CH_2CH_3)_4]^+$ cations and SO_2ClF are given in Tables S1−S6 of the Supporting Information. The cations and SO_2ClF parameters are in good agreement with previously published values[37−41] and do not require further comment.

(a) $[N(CH_2CH_3)_4]_2[Hg(OTeF_5)_4]$. The crystal structure of $[N(CH_2CH_3)_4]_2[Hg(OTeF_5)_4]$ (Figure 1 and Figure S1, Supporting Information) consists of well-isolated $[Hg(OTeF_5)_4]^{2-}$ anions and $[N(CH_2CH_3)_4]^+$ cations, with the shortest F---CH_3 distances (3.178(12)−3.398(11) Å) being near the sum of the F[42] and CH_3[43] van der Waals radii (3.47 Å) and equally distributed among the four F_5TeO- groups. The anion geometry closely approximates the calculated gas-phase structure (see Computational Details), which is consistent with minimal and well-dispersed cation−anion interactions. The Hg(II)

DOI: 10.1021/ic502602p
Inorg. Chem. 2015, 54, 1606−1626

Table 1. Summary of Crystal Data and Refinement Results for $[N(CH_2CH_3)_4]_2[Hg(OTeF_5)_4]$, $[N(CH_3)_4]_3[Hg(OTeF_5)_5]$, $[N(CH_2CH_3)_4]_3[Hg(OTeF_5)_5]$, $[N(CH_3)_4]_2[Hg_2(OTeF_5)_6]$, $Cs_2[Hg(OTeF_5)_4]\cdot Hg(OTeF_5)_2$, and $\{Cs_3[Hg_2(OTeF_5)_7]\cdot Hg(OTeF_5)_2\}\cdot 4SO_2ClF$

	$[N(CH_2CH_3)_4]_2[Hg(OTeF_5)_4]$	$[N(CH_3)_4]_3[Hg(OTeF_5)_5]$	$[N(CH_2CH_3)_4]_3[Hg(OTeF_5)_5]$	$[N(CH_3)_4]_2[Hg_2(OTeF_5)_6]$	$Cs_2[Hg(OTeF_5)_4]\cdot Hg(OTeF_5)_2$	$\{Cs_3[Hg_2(OTeF_5)_7]\cdot Hg(OTeF_5)_2\}\cdot 4SO_2ClF$
space group	*Pc*	*Cc*	$P2_1$	$P2_1/c$	$C2/c$	$P2_1/c$
a (Å)	10.4748(6)	16.207(2)	14.5473(2)	19.7463 (3)	22.6115(3)	20.5000(4)
b (Å)	13.4264(7)	14.455(1)	17.9914(2)	11.4754 (2)	10.9340(2)	13.8017(3)
c (Å)	16.2322(7)	16.248(1)	18.7584(2)	18.0628(3)	15.2294(4)	22.1592(4)
β (deg)	127.345(2)	90.172(3)	95.265(1)	109.147(1)	125.797(1)	107.729(1)
V (Å^3)	1814.9(2)	3806.7(6)	4888.9(1)	3866.6(1)	3053.8(1)	5971.8(2)
molecules/unit cell	2	4	4	8	8	4
mol wt (g mol^{-1})	1415.49	1616.03	1784.34	990.54	1049.30	3621.94
calcd density (g cm^{-3})	2.590	2.820	2.424	3.403	4.564	4.028
T (°C)	−173	−173	−173	−173	−173	−173
μ (mm^{-1})	7.52	7.95	6.20	12.54	18.21	14.33
R_1[a]	0.0285	0.0196	0.0282	0.0194	0.0216	0.0514
wR_2[b]	0.0632	0.0423	0.0465	0.0403	0.0436	0.1122

[a] R_1 is defined as $\sum ||F_0| - |F_c||/\sum |F_0|$ for $I > 2\sigma(I)$. [b] wR_2 is defined as $[\sum[w(F_0^2 - F_c^2)^2]/\sum w(F_0^2)^2]^{1/2}$ for $I > 2\sigma(I)$.

Table 2. Selected Experimental Geometrical Parameters for the $[Hg(OTeF_5)_4]^{2-}$ Anion in $[N(CH_2CH_3)_4]_2[Hg(OTeF_5)_4]$ and Selected Calculated Geometrical Parameters for $[Hg(OTeF_5)_4]^{2-}$

exptl (C_1)[a]		calcd (S_4)[b]	
	Bond Lengths (Å)		
$Hg_{(1)}-O_{(1)}$	2.214(6)	Hg_1-O_8	2.226
$Hg_{(1)}-O_{(2)}$	2.229(7)	Hg_1-O_{14}	2.226
$Hg_{(1)}-O_{(3)}$	2.275(7)	Hg_1-O_{18}	2.226
$Hg_{(1)}-O_{(4)}$	2.146(7)	Hg_1-O_{28}	2.226
Te−O	1.788(6)−1.805(7)	Te−O	1.799
Te−F	1.816(6)−1.861(6)	Te−F	1.864−1.871
	Bond angles (deg)		
$O_{(1)}-Hg_{(1)}-O_{(2)}$	96.8(3)	$O_8-Hg_1-O_{14}$	108.0
$O_{(1)}-Hg_{(1)}-O_{(3)}$	96.6(2)	$O_8-Hg_1-O_{18}$	112.4
$O_{(1)}-Hg_{(1)}-O_{(4)}$	120.1(3)	$O_8-Hg_1-O_{28}$	108.0
$O_{(2)}-Hg_{(1)}-O_{(3)}$	86.3(2)	$O_{14}-Hg_1-O_{18}$	108.0
$O_{(2)}-Hg_{(1)}-O_{(4)}$	125.9(3)	$O_{14}-Hg_1-O_{28}$	112.4
$O_{(3)}-Hg_{(1)}-O_{(4)}$	122.8(3)	$O_{18}-Hg_1-O_{28}$	108.0

[a] The atom labeling scheme corresponds to that used in Figure 1 and Figure S1 of the Supporting Information. [b] Calculated at the PBE1PBE/def2-TVZPP level of theory. The atom labeling scheme corresponds to that used in Figure 10a.

coordination sphere is a distorted tetrahedron with O−Hg−O bond angles ranging from 86.3(2) to 125.9(3)°. The $[B(OTeF_5)_4]^-$ anion[29] is the only other tetrahedrally coordinated teflate anion that has been structurally characterized by single-crystal X-ray diffraction; however, $[Hg(OTeF_5)_4]^{2-}$ is significantly more distorted than $[B(OTeF_5)_4]^-$ (∠O−B−O, 106.8(3)−113.8(3)°)[30] or $C(OTeF_5)_4$ (∠O−C−O, 105(1)−116(1)°).[30] Although the isovalent $[Zn(OTeF_5)_4]^{2-}$ anion has been referred to in the literature,[35,36] its crystal structure has not been reported. The $[Pd(OTeF_5)_4]^{2-}$ anion has been characterized by single-crystal X-ray diffraction, but the anion is not well isolated in the crystal structure. Instead, the square-planar PdO_4 moiety is O-bridged to two $[Ag(C_nH_{2n}Cl_2)_2]^+$ (n = 1, 2) cations.[44] The Hg−O bond lengths of $[Hg(OTeF_5)_4]^{2-}$ (2.146(7)−2.275(7) Å) are slightly longer than those of $Hg(OTeF_5)_2$ (2.016(6) Å).[27] Because of its negative charge, the Hg−O bonds of $[Hg(OTeF_5)_4]^{2-}$ are expected to be longer and more polar than those of neutral $Hg(OTeF_5)_2$ (see Computational Results and NBO sections). Increases in the Hg−O bond lengths are paralleled by decreases in the Te−O bond lengths ($[Hg(OTeF_5)_4]^{2-}$, 1.788(6)−1.805(7) Å; $Hg(OTeF_5)_2$, 1.842(7) Å),[27] which have more π character and are comparable to that of $[C_{14}H_{19}N_2][OTeF_5]$ (1.803 Å). The Te−O bond lengths are shorter than in any other anion containing terminally bonded F_5TeO- groups, i.e., $[Nb(OTeF_5)_6]^-$ (1.806(9)−1.824(7) Å),[34] $[Ti(OTeF_5)_6]^{2-}$, (1.812(9)−1.822(7) Å),[34] $[B(OTeF_5)_4]^-$ (1.828(2)−1.834(2) Å),[30] and $[Pn(OTeF_5)_6]^-$ (Pn = Sb, 1.832(7)−1.849(7) Å,[34] and Bi, 1.846(6)−1.860(6) Å.[33] The Te−F bond lengths ($Te-F_{ax}$, 1.816(6)−1.832(6) Å and $Te-F_{eq}$, 1.832(6)−1.861(6) Å) are slightly longer than those of $Hg(OTeF_5)_2$ ($Te-F_{ax}$, 1.819(6) Å and $Te-F_{eq}$, 1.824(6)−1.839(6) Å),[27] which is consistent with the increased negative charges on the oxygen atoms and shorter Te−O bond lengths. These trends are reproduced by the calculated geometries and are reflected in the NBO analyses (see Computational Results).

(b) $[N(CH_3)_4]_3[Hg(OTeF_5)_5]$ and $[N(CH_2CH_3)_4]_3[Hg(OTeF_5)_5]$. The crystal structure of $[N(CH_3)_4]_3[Hg(OTeF_5)_5]$ (Figure 2 and Figure S2, Supporting Information) consists of well-isolated

DOI: 10.1021/ic502602p
Inorg. Chem. 2015, 54, 1606−1626

Table 3. Selected Experimental Geometrical Parameters for the $[Hg(OTeF_5)_5]^{3-}$ Anion in $[N(CH_3)_4]_3[Hg(OTeF_5)_5]$ and $[N(CH_2CH_3)_4]_3[Hg(OTeF_5)_5]$, and Selected Calculated Geometrical Parameters for $[Hg(OTeF_5)_5]^{3-}$

exptl (C_1)						calcd (C_1)[c]	
$[N(CH_3)_4]^+$ [a]				$[N(CH_2H_3)_4]^+$ [b]			
Bond Lengths (Å)							
$Hg_{(1)}-O_{(1)}$	2.318(5)	$Hg_{(1)}-O_{(2)}$	2.317(3)	$Hg_{(2)}-O_{(6)}$	2.297(3)	Hg_1-O_8	2.481
$Hg_{(1)}-O_{(3)}$	2.301(5)	$Hg_{(1)}-O_{(3)}$	2.313(3)	$Hg_{(2)}-O_{(9)}$	2.319(3)	Hg_1-O_{12}	2.510
$Hg_{(1)}-O_{(4)}$	2.323(4)	$Hg_{(1)}-O_{(5)}$	2.276(3)	$Hg_{(2)}-O_{(10)}$	2.290(3)	Hg_1-O_{25}	2.482
$Hg_{(1)}-O_{(2)}$	2.227(5)	$Hg_{(1)}-O_{(1)}$	2.265(3)	$Hg_{(2)}-O_{(7)}$	2.262(3)	Hg_1-O_{34}	2.111
$Hg_{(1)}-O_{(5)}$	2.230(5)	$Hg_{(1)}-O_{(4)}$	2.259(3)	$Hg_{(2)}-O_{(8)}$	2.266(3)	Hg_1-O_{22}	2.110
$Hg_{(1)}\cdots F_{(17)}$	3.008(4)	$Hg_{(1)}\cdots F_{(17)}$	3.141(3)	$Hg_{(2)}\cdots F_{(46)}$	3.133(3)		
Te−O	1.772(5)−1.801(4)	Te−O	1.782(3)−1.795(3)	Te−O	1.777(3)−1.795(3)	Te−O	1.777−1.779
Te−F	1.837(5)−1.863(4)	Te−F	1.844(3)−1.860(3)	Te−F	1.832(4)−1.865(3)	Te−F	1.854−1.891
Bond Angles (deg)							
$O_{(1)}-Hg_{(1)}-O_{(2)}$	95.7(2)	$O_{(1)}-Hg_{(1)}-O_{(2)}$	116.4(1)	$O_{(6)}-Hg_{(2)}-O_{(7)}$	86.5(1)	$O_8-Hg_1-O_{12}$	122.1
$O_{(1)}-Hg_{(1)}-O_{(3)}$	96.4(1)	$O_{(1)}-Hg_{(1)}-O_{(3)}$	104.6(1)	$O_{(6)}-Hg_{(2)}-O_{(8)}$	108.9(1)	$O_8-Hg_1-O_{22}$	88.2
$O_{(1)}-Hg_{(1)}-O_{(4)}$	156.3(2)	$O_{(1)}-Hg_{(1)}-O_{(4)}$	102.3(1)	$O_{(6)}-Hg_{(2)}-O_{(9)}$	145.9(1)	$O_8-Hg_1-O_{25}$	115.8
$O_{(1)}-Hg_{(1)}-O_{(5)}$	84.3(2)	$O_{(1)}-Hg_{(1)}-O_{(5)}$	88.1(1)	$O_{(6)}-Hg_{(2)}-O_{(10)}$	87.6(1)	$O_8-Hg_1-O_{34}$	89.9
$O_{(2)}-Hg_{(1)}-O_{(3)}$	94.8(2)	$O_{(2)}-Hg_{(1)}-O_{(3)}$	138.6(1)	$O_{(7)}-Hg_{(2)}-O_{(8)}$	107.5(1)	$O_{12}-Hg_1-O_{22}$	91.8
$O_{(2)}-Hg_{(1)}-O_{(4)}$	83.5(2)	$O_{(2)}-Hg_{(1)}-O_{(4)}$	88.3(1)	$O_{(7)}-Hg_{(2)}-O_{(9)}$	87.8(1)	$O_{12}-Hg_1-O_{25}$	122.1
$O_{(2)}-Hg_{(1)}-O_{(5)}$	161.6(2)	$O_{(2)}-Hg_{(1)}-O_{(5)}$	88.0(1)	$O_{(7)}-Hg_{(2)}-O_{(10)}$	161.5(1)	$O_{12}-Hg_1-O_{34}$	91.8
$O_{(3)}-Hg_{(1)}-O_{(4)}$	107.3(2)	$O_{(3)}-Hg_{(1)}-O_{(4)}$	88.3(1)	$O_{(8)}-Hg_{(2)}-O_{(9)}$	104.9(1)	$O_{22}-Hg_1-O_{25}$	89.9
$O_{(3)}-Hg_{(1)}-O_{(5)}$	103.5(2)	$O_{(3)}-Hg_{(1)}-O_{(5)}$	88.1(1)	$O_{(8)}-Hg_{(2)}-O_{(10)}$	91.0(1)	$O_{22}-Hg_1-O_{34}$	176.4
$O_{(4)}-Hg_{(1)}-O_{(5)}$	89.2(2)	$O_{(4)}-Hg_{(1)}-O_{(5)}$	169.5(1)	$O_{(9)}-Hg_{(2)}-O_{(10)}$	87.4(1)	$O_{25}-Hg_1-O_{34}$	88.3

[a]The atom labeling scheme corresponds to that used in Figure 2 and Figure S2 of the Supporting Information. [b]The atom labeling scheme corresponds to that used in Figure S3 of the Supporting Information. [c]Calculated at the PBE1PBE/def2-TVZPP level of theory. The atom labeling scheme corresponds to that used in Figure 10b.

DOI: 10.1021/ic502602p
Inorg. Chem. 2015, 54, 1606−1626

Table 4. Selected Experimental Geometrical Parameters for $[Hg_2(OTeF_5)_6]^{2-}$ in $[N(CH_3)_4]_2[Hg_2(OTeF_5)_6]$ and Selected Calculated Geometrical Parameters for $[Hg_2(OTeF_5)_6]^{2-}$

exptl (C_1)[a]		calcd (D_2)[b]	
Bond Lengths (Å)			
$Hg_{(1)}-O_{(4)}$	2.040(4)	Hg_1-O_{37}	2.081
$Hg_{(1)}-O_{(3)}$	2.062(4)	Hg_1-O_{22}	2.081
$Hg_{(1)}-O_{(5)}$	2.486(4)	Hg_1-O_{34}	2.441
$Hg_{(1)}-O_{(2)}$	2.508(4)	Hg_1-O_{24}	2.441
$Hg_{(1)}\cdots F_{(4A)}$	2.850(3)		
$Hg_{(1)}\cdots F_{(11)}$	3.093(4)		
$Hg_{(2)}-O_{(1)}$	2.075(4)	Hg_2-O_{36}	2.081
$Hg_{(2)}-O_{(6)}$	2.104(5)	Hg_2-O_{39}	2.081
$Hg_{(2)}-O_{(5)}$	2.350(4)	Hg_2-O_{34}	2.441
$Hg_{(2)}-O_{(2)}$	2.416(4)	Hg_2-O_{24}	2.441
$Hg_{(2)}\cdots F_{(18)}$	2.813(4)		
$Hg_{(2)}\cdots F_{(3)}$	3.214(4)		
$Te_{(1)}-O_{(1)}$	1.816(4)	Te_3-O_{36}	1.821
$Te_{(2)}-O_{(2)}$	1.790(4)	Te_5-O_{24}	1.810
$Te_{(3)}-O_{(3)}$	1.821(4)	Te_6-O_{22}	1.821
$Te_{(4)}-O_{(4)}$	1.812(4)	Te_4-O_{37}	1.821
$Te_{(5)}-O_{(5)}$	1.802(4)	Te_7-O_{34}	1.810
$Te_{(6)}-O_{(6)}$	1.809(5)	Te_8-O_{39}	1.821
Te−F[c]	1.825(3)−1.858(3)	Te−F	1.853−1.865
Bond Angles (deg)			
$Hg_{(1)}-O_{(2)}-Hg_{(2)}$	102.1(1)	$Hg_1-O_{24}-Hg_2$	107.2
$Hg_{(1)}-O_{(5)}-Hg_{(2)}$	104.7(1)	$Hg_1-O_{34}-Hg_2$	107.2
$O_{(2)}-Hg_{(1)}-O_{(5)}$	70.0(1)	$O_{24}-Hg_1-O_{34}$	72.8
$O_{(3)}-Hg_{(1)}-O_{(4)}$	174.1(2)	$O_{22}-Hg_1-O_{37}$	162.5
$O_{(3)}-Hg_{(1)}-O_{(2)}$	85.4(2)	$O_{22}-Hg_1-O_{24}$	96.5
$O_{(3)}-Hg_{(1)}-O_{(5)}$	87.2(2)	$O_{22}-Hg_1-O_{34}$	97.6
$O_{(4)}-Hg_{(1)}-O_{(2)}$	98.3(2)	$O_{37}-Hg_1-O_{24}$	97.6
$O_{(4)}-Hg_{(1)}-O_{(5)}$	98.4(2)	$O_{37}-Hg_1-O_{34}$	72.8
$O_{(2)}-Hg_{(2)}-O_{(5)}$	73.9(1)	$O_{24}-Hg_2-O_{34}$	72.80
$O_{(1)}-Hg_{(2)}-O_{(6)}$	157.0(2)	$O_{36}-Hg_2-O_{39}$	162.5
$O_{(1)}-Hg_{(2)}-O_{(2)}$	99.2(2)	$O_{36}-Hg_2-O_{24}$	97.6
$O_{(1)}-Hg_{(2)}-O_{(5)}$	108.6(2)	$O_{36}-Hg_2-O_{34}$	96.5
$O_{(6)}-Hg_{(2)}-O_{(2)}$	93.7(2)	$O_{39}-Hg_2-O_{24}$	96.5
$O_{(6)}-Hg_{(2)}-O_{(5)}$	93.2(2)	$O_{39}-Hg_2-O_{34}$	97.6
Dihedral Angles (deg)			
$Te_{(3)}-O_{(3)}-Hg_{(1)}-O_{(4)}-Te_{(4)}$	122.3(3)	$Te_6-O_{22}-Hg_1-O_{37}-Te_4$	12.1
$Te_{(1)}-O_{(1)}-Hg_{(2)}-O_{(6)}-Te_{(6)}$	34.7(5)	$Te_3-O_{36}-Hg_2-O_{39}-Te_8$	12.1

[a]The atom labeling scheme corresponds to that used in Figure 3 and Figure S4 of the Supporting Information. [b]Calculated at the PBE1PBE/def2-TVZPP level of theory. The atom labeling scheme corresponds to that used in Figure 10c. [c]Bond lengths associated with the disordered F_5TeO- group are not included.

$[Hg(OTeF_5)_5]^{3-}$ anions and $[N(CH_3)_4]^+$ cations, where the shortest F---CH_3 cation−anion distances (3.094(9)−3.406(9) Å) are near the sum of the F[42] and CH_3[43] van der Waals radii. In contrast with $[N(CH_2CH_3)_4]_2[Hg(OTeF_5)_4]$, the long F---$CH_3$ cation−anion interactions are not equally distributed among the teflate groups, with the largest number of the F---CH_3 interactions occurring between three F_5TeO- groups ($F_5Te_{(1)}O$, $F_5Te_{(4)}O$, and $F_5Te_{(3)}O$), causing the bond pair arrangement around the central Hg atom to deviate significantly from that of the ideal trigonal bipyramidal geometry that is predicted by the VSEPR rules[45] for the gas-phase anion (see Computational Details). The $O_{(1)}-Hg-O_{(4)}$ angle (156.3(2)°), which should be equal to the $O_{(1)}-Hg-O_{(3)}$ (96.4(1)°) and $O_{(4)}-Hg-O_{(3)}$ (107.3(2)°) angles in a trigonal bipyramid, is splayed open such that $O_{(1)}$ and $O_{(4)}$ become essentially coplanar with $O_{(2)}$ and $O_{(5)}$ (with $O_{(1)}$ and $O_{(4)}$ positioned −0.062 Å below the average $O_{(1)}O_{(4)}O_{(2)}O_{(5)}$-plane and $O_{(2)}$ and $O_{(5)}$ positioned +0.061 Å above this plane), giving a Hg(II) coordination sphere that is best described as a distorted square pyramid. This description is supported by the anion's τ-parameter ($\tau = |\beta - \alpha|/60$), where β and α are the two largest angles involving different oxygen ligand atoms,[46] i.e., $O_{(1)}-Hg-O_{(4)}$ (156.3(2)°) and $O_{(2)}-Hg-O_{(5)}$ (161.6(2)°). The τ-parameter can range from 0 to 1 and is used as a quantitative measure of how closely the geometry approximates either a trigonal bipyramid (ideal value, 1) or a square pyramid (ideal value, 0). In the present case, $\tau = 0.088$ where the $O_{(3)}$ atom is in the axial position and the remaining oxygen atoms ($O_{(1)}$, $O_{(2)}$, $O_{(4)}$, and $O_{(5)}$) form the equatorial plane of the square pyramid. The Hg(II) atom is +0.411 Å above the average $O_{(1)}O_{(4)}O_{(2)}O_{(5)}$-plane and the $Hg-O_{eq}$ bonds in the equatorial plane are bent away from the axial oxygen, $O_{(3)}$; consequently, the $O_{eq}-Hg-O_{(3)}$ bond angles (94.8(2)−107.3(2)°) are larger than 90°. The *cis*-$O_{eq}-Hg-O_{eq}$ bond angles range from 83.5(2) to 95.7(2)°. There are two groups of $Hg-O_{eq}$ bonds, two shorter

DOI: 10.1021/ic502602p
Inorg. Chem. 2015, 54, 1606−1626

Table 5. Selected Experimental Geometrical Parameters for $Cs_2[Hg(OTeF_5)_4]\cdot Hg(OTeF_5)_2$ and Selected Calculated Geometrical Parameters for $[Hg_3(OTeF_5)_8]^{2-}$

exptl $Cs_2[Hg(OTeF_5)_4]\cdot Hg(OTeF_5)_2$ (C_1) [a]		calcd $[Hg_3(OTeF_5)_8]^{2-}$ (C_1) [b]	
Bond Lengths (Å)			
$Hg_{(1)}-O_{(2)}$	2.058(2)	Hg_2-O_{24}	2.040
		Hg_2-O_{23}	2.040
		$Hg_{45}-O_{46}$	2.040
		$Hg_{45}-O_{47}$	2.041
$Hg_{(1)}\cdots O_{(3)}$	2.555(1)	$Hg_2\cdots O_{31}$	2.560
$Hg_{(1)}\cdots O_{(1)}$	2.737(1)	$Hg_2\cdots O_{17}$	2.558
		$Hg_{45}\cdots O_{16}$	2.564
		$Hg_{45}\cdots O_{32}$	2.554
$Hg_{(2)}-O_{(1)}$	2.186(1)	Hg_1-O_{16}	2.228
$Hg_{(2)}-O_{(3)}$	2.287(1)	Hg_1-O_{17}	2.238
		Hg_1-O_{31}	2.231
		Hg_1-O_{32}	2.241
$Hg_{(2)}\cdots F_{(6)}$	2.731(1)		
Te–O	1.798(1)–1.816(1)	Te–O	1.823–1.824
Te–F	1.841(1)–1.863(1)	Te–F	1.823–1.866
Bond Angles (deg)			
$O_{(2)}-Hg_{(1)}-O_{(2A)}$	180.0	$O_{23}-Hg_2-O_{24}$	172.2
		$O_{46}-Hg_{45}-O_{47}$	172.0
$O_{(2)}-Hg_{(1)}\cdots O_{(3)}$	86.7(1)	$O_{23}-Hg_2\cdots O_{31}$	92.4
		$O_{24}-Hg_2\cdots O_{31}$	94.2
$O_{(2)}-Hg_{(1)}\cdots O_{(3A)}$	93.2(1)	$O_{23}-Hg_2\cdots O_{17}$	96.3
		$O_{24}-Hg_2\cdots O_{17}$	90.1
$O_{(2)}-Hg_{(1)}\cdots O_{(1)}$	106.6(1)		
$O_{(2)}-Hg_{(1)}\cdots O_{(1A)}$	73.4(1)	$O_{46}-Hg_{45}\cdots O_{16}$	90.9
$O_{(2)}-Hg_{(1)}\cdots O_{(3A)}$	93.2(1)	$O_{47}-Hg_{45}\cdots O_{32}$	92.5
		$O_{46}-Hg_{45}\cdots O_{32}$	93.9
		$O_{47}-Hg_{45}\cdots O_{16}$	96.1
$O_{(1)}-Hg_{(2)}-O_{(3)}$	110.4(1)	$O_{16}-Hg_1-O_{17}$	126.8
		$O_{16}-Hg_1-O_{31}$	128.7
$O_{(1)}-Hg_{(2)}-O_{(3A)}$	81.4(1)	$O_{16}-Hg_1-O_{32}$	77.8
$O_{(1)}-Hg_{(2)}-O_{(1A)}$	147.8(1)	$O_{17}-Hg_1-O_{31}$	77.8
$O_{(3)}-Hg_{(2)}-O_{(3A)}$	137.9(1)	$O_{17}-Hg_1-O_{32}$	127.0
		$O_{31}-Hg_1-O_{32}$	126.6
Dihedral Angles (deg)			
$Te_{(2)}-O_{(2)}-Hg_{(1)}-O_{(2A)}-Te_{(2A)}$	0.0	$Te_5-O_{23}-Hg_2-O_{24}-Te_{25}$	2.2
		$Te_{48}-O_{46}-Hg_{45}-O_{47}-Te_{49}$	15.0

[a]The atom labeling scheme corresponds to that used in Figure 4 and Figure S5 of the Supporting Information. [b]Calculated at the PBE1PBE/def2-TVZPP level of theory. The atom labeling scheme corresponds to that used in Figure 10d.

trans-bonds (2.227(5) and 2.230(5) Å), and two longer *trans*-bonds (2.318(5) and 2.323(4) Å); the axial $Hg-O_{(3)}$ bond length is intermediate (2.301(5) Å). The two equatorial *trans*-$OTeF_5$ groups, $F_5Te_{(1)}O-$ and $F_5Te_{(4)}O-$, point away from the axial $F_5Te_{(3)}O-$ group, adopting a *trans*, *syn*-conformation relative to one another. The $F_5Te_{(5)}O-$ group adopts a *cis*, *anti*-conformation relative to the $F_5Te_{(1)}O-$ and $F_5Te_{(4)}O-$ groups, whereas the $F_5Te_{(2)}O-$ group adopts a *cis*, *gauche*-conformation in order to avoid the apical $F_5Te_{(3)}O-$ group, which points toward the midpoint of a straight line drawn between $O_{(2)}$ and $O_{(4)}$ of the $F_5Te_{(2)}O-$ and $F_5Te_{(4)}O-$ groups. The Hg–O bonds are slightly longer than those in $[Hg(OTeF_5)_4]^{2-}$ (see above). The Hg–O bond lengths elongate, and the Hg–O valencies decrease with increasing negative charge and the number of F_5TeO- groups, i.e., 2.016(6) Å ($Hg(OTeF_5)_2$) < 2.146(7)–2.275(7) Å ($[Hg(OTeF_5)_4]^{2-}$) < 2.227(5)–2.323(4) Å ($[Hg(OTeF_5)_5]^{3-}$) (see Computational Results and NBO sections). The Te–O (1.772(5)–1.801(4) Å) and Te–F (1.837(5)–1.863(4) Å) bond lengths are comparable to those in $[Hg(OTeF_5)_4]^{2-}$ (Te–O, 1.788(6)–1.805(7) Å and Te–F, 1.819(6)–1.839(6) Å). An additional long $Hg_{(1)}\cdots F_{(17)}$ (3.008(9) Å) intra-ionic contact occurs *trans* to $Hg\cdots O_{(3)}$, which may favor the observed square-pyramidal geometry. In the crystal structure of $[N(CH_2CH_3)_4]_3[Hg(OTeF_5)_5]$ (Figure S3, Supporting Information), the τ parameters for the two crystallographically distinct $[Hg(OTeF_5)_5]^{3-}$ anions are 0.260 and 0.515, indicating that the anion geometries are intermediate with respect to the square-pyramidal anion geometry in the $[N(CH_3)_4]^+$ salt and the trigonal-bipyramidal gas-phase geometry. Long $Hg_{(1)}\cdots F_{(17)}$ (3.141(2) Å) and $Hg_{(2)}\cdots F_{(46)}$ (3.133(2) Å) intra-ionic contacts analogous to the $Hg_{(1)}\cdots F_{(17)}$ contacts in the $[N(CH_3)_4]^+$ salt also occur for each anion and also favor the square-pyramidal geometry.

The only other known pentacoordinate teflate anion is $[Te(OTeF_5)_5]^-$.[32] In this instance, the geometry of the Te(IV) coordination sphere is dictated by the presence of a tellurium valence electron lone pair that results in a distorted octahedral arrangement of five bond pairs and one electron lone pair in the Te(IV) valence shell. The geometry around Te(IV) is also a distorted square pyramid but differs from that of $[Hg(OTeF_5)_5]^{3-}$, with $O_{ax}-Te-O_{eq}$ bond angles that are less than 90° and equatorial oxygen atoms that are displaced toward the axial oxygen atom so that the central Te atom is positioned below the equatorial plane of oxygen atoms. The displacement is caused by electron lone pair–equatorial electron bond pair interactions in the Te(IV) valence shell.

(c) $[N(CH_3)_4]_2[Hg_2(OTeF_5)_6]$. The crystal structure of $[N(CH_3)_4]_2[Hg_2(OTeF_5)_6]$ consists of $[N(CH_3)_4]^+$ cations and dimeric $[Hg_2(OTeF_5)_6]^{2-}$ anions (Figure 3 and Figure S4, Supporting Information). The anions pack along the *c*-axis and interact with each other through weak Hg---F contacts ($Hg_{(1)}\cdots F_{(4A)}$, 2.850(3) Å and $Hg_{(2)}\cdots F_{(18B)}$, 2.812(4) Å). Two additional long $Hg_{(1)}\cdots F_{(11)}$ (3.093(4) Å) and $Hg_{(2)}\cdots F_{(3)}$ (3.214(4) Å) intra-ionic contacts contribute to the distorted octahedral coordination spheres of $Hg_{(1)}$ and $Hg_{(2)}$ (Figure S4, Supporting Information). Each anion is comprised of two crystallographically inequivalent $Hg(OTeF_5)_2$ molecules that are linked

DOI: 10.1021/ic502602p
Inorg. Chem. 2015, 54, 1606–1626

Table 6. Selected Experimental Geometrical Parameters for $\{Cs_3[Hg_2(OTeF_5)_7]\cdot Hg(OTeF_5)_2\}\cdot 4SO_2ClF$[a]

		Bond Lengths (Å)	
$Hg_{(1)}-O_{(4)}$	2.059(5)	$Hg_{(3)}-O_{(9)}$	2.211(5)
$Hg_{(1)}-O_{(5)}$	2.073(5)	$Hg_{(3)}-O_{(8)}$	2.234(5)
$Hg_{(1)}\cdots O_{(6)}$	2.605(5)	$Hg_{(3)}-O_{(6)}$	2.266(5)
$Hg_{(1)}\cdots O_{(7)}$	2.529(5)	$Hg_{(3)}-O_{(3)}$	2.369(5)
$Hg_{(1)}\cdots O_{(8)}$	2.653(5)	$Hg_{(3)}\cdots O_{(1}$	2.631(5)
$Hg_{(1)}\cdots O_{(2)}$	2.737(5)	$Hg_{(3)}\cdots F_{(21)}$	2.675(5)
$Hg_{(2)}-O_{(1)}$	2.169(5)		
$Hg_{(2)}-O_{(2)}$	2.156(5)	Te−O	1.801(5)−1.816(5)
$Hg_{(2)}-O_{(3)}$	2.356(5)		
$Hg_{(2)}-O_{(7)}$	2.359(5)	Te−F	1.830(5)−1.860(5)
$Hg_{(2)}\cdots O_{(9)}$	2.680(5)		
$Hg_{(2)}\cdots F_{(16)}$	2.668(5)		
		Bond Angles (deg)	
$O_{(4)}-Hg_{(1)}-O_{(5)}$	174.7(2)	$Hg_{(2)}-O_{(1)}\cdots Hg_{(3)}$	134.0(2)
$Hg_{(2)}-O_{(3)}-Hg_{(3)}$	96.(2)	$Hg_{(2)}\cdots O_{(9)}-Hg_{(3)}$	91.7(2)
$O_{(1)}-Hg_{(2)}-O_{(2)}$	156.4(2)	$O_{(9)}-Hg_{(3)}-O_{(8)}$	127.2(2)
$O_{(1)}-Hg_{(2)}-O_{(3)}$	75.0(2)	$O_{(9)}-Hg_{(3)}-O_{(6)}$	127.2(2)
$O_{(1)}-Hg_{(2)}-O_{(7)}$	108.4(2)	$O_{(9)}-Hg_{(3)}-O_{(3)}$	79.1(2)
$O_{(2)}-Hg_{(2)}-O_{(3)}$	117.4(2)	$O_{(8)}-Hg_{(3)}-O_{(6)}$	81.2(2)
$O_{(2)}-Hg_{(2)}-O_{(7)}$	79.4(2)	$O_{(8)}-Hg_{(3)}-O_{(3)}$	149.2(2)
$O_{(3)}-Hg_{(2)}-O_{(7)}$	130.8(2)	$O_{(6)}-Hg_{(3)}-O_{(3)}$	95.3(2)
		Dihedral Angles (deg)	
$Te_{(4)}-O_{(4)}-Hg_{(1)}-O_{(5)}-Te_{(5)}$		150.9 (4)	

[a]The atom labeling scheme corresponds to that used in Figure 5 and Figure S6 of the Supporting Information.

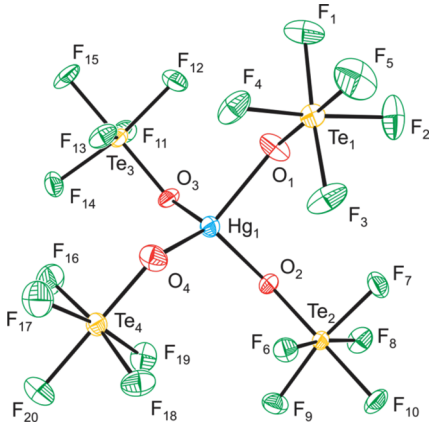

Figure 1. The $[Hg(OTeF_5)_4]^{2-}$ anion in the X-ray crystal structure of $[N(CH_2CH_3)_4]_2[Hg(OTeF_5)_4]$ with thermal ellipsoids shown at the 50% probability level.

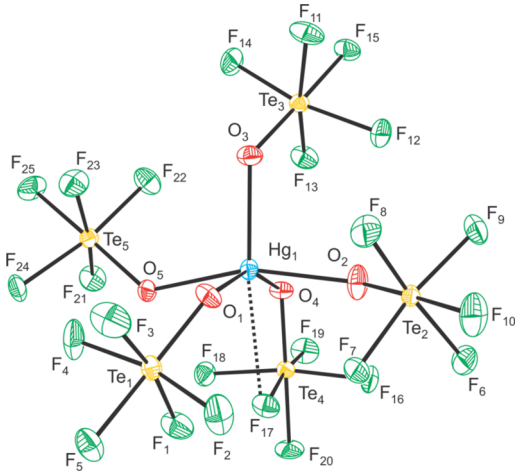

Figure 2. The $[Hg(OTeF_5)_5]^{3-}$ anion in the X-ray crystal structure of $[N(CH_3)_4]_3[Hg(OTeF_5)_5]$, where the $Hg_{1}\cdots F_{17}$ contact is indicated by a dashed line. Thermal ellipsoids are shown at the 50% probability level.

to two crystallographically inequivalent bridging bidentate $F_5TeO_\mu-$ groups to form a $[HgO_\mu]_2$ core. The $[N(CH_3)_4]^+$ cations weakly interact with the anions; the shortest $F\cdots CH_3$ (2.949(8)−3.394(7) Å) distances being less than or near the sum of the F [42] and CH_3 [43] van der Waals radii (Table S3, Supporting Information).

The Hg and O_μ atoms are not coplanar, with the two Hg atoms positioned +0.24 Å above the average $HgO_\mu HgO_\mu$ plane, and the two O_μ atoms positioned −0.24 Å below this plane. The result is a butterfly-shaped $[HgO_\mu]_2$ geometry having $Hg-O_\mu-Hg$ angles of 102.1(1)° and 104.6(1)° and $O_\mu-Hg-O_\mu$ angles of 70.1(1)° and 73.9(1)°. Similar dimeric $[MO_\mu]_2$ core structures have been observed in $[AgOTeF_5(1,2\text{-}C_2H_4Cl_2)]$,[22] $[TlOTeF_5(mes)_2]_2\cdot mes$,[20] and $[Zn(OTeF_5)_2(C_6H_5NO_2)_2]_2$;[24] however, $[Hg_2(OTeF_5)_6]^{2-}$ is the first anionic example. Each Hg(II) atom is coordinated to two terminal F_5TeO_t- groups and two bridging $F_5TeO_\mu-$ groups. The $Hg_{(1)}-O_t$ bond lengths of the F_5TeO_t- groups ($O_{(3)}$, 2.064(4) and $O_{(4)}$, 2.044(4) Å) are comparable to those of $Hg(OTeF_5)_2$ (2.016(6) Å), whereas the $Hg_{(2)}-O_t$ bond lengths ($O_{(1)}$, 2.074(4) and $O_{(6)}$, 2.103(4) Å) are slightly elongated. As expected, the $Hg-O_\mu$ bonds are longer than the $Hg-O_t$ bonds, with the bridging $Hg_{(1)}-O_\mu$ bonds ($O_{(2)}$, 2.507(4) and $O_{(5)}$, 2.486(4) Å), being slightly elongated with respect to the $Hg_{(2)}-O_\mu$ bridge bonds ($O_{(2)}$, 2.417(4) and $O_{(5)}$, 2.353(4) Å). Analogous Zn−O bond length trends have been observed in $[Zn(OTeF_5)_2(C_6H_5NO_2)_2]_2$ ($Zn-O_t$ (1.928(7) Å) < $Zn-O_\mu$ (2.012(5) Å).[24] The $O_{(3)}-Hg_{(1)}-O_{(4)}$ bond angle (174.1(2)°) is similar to that of $Hg(OTeF_5)_2$ (170.5(4)°),[27] whereas the $O_{(1)}-Hg_{(2)}-O_{(6)}$ bond angle (157.0(2)°) is smaller. As observed in both solid- and gas-phase $Hg(OTeF_5)_2$, the $Hg-O_t$ bonds are *trans* to one

DOI: 10.1021/ic502602p
Inorg. Chem. 2015, 54, 1606−1626

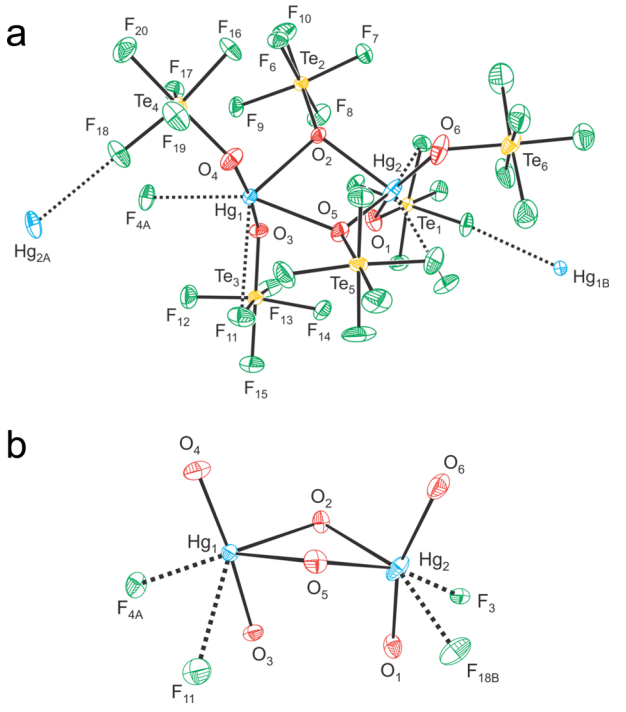

Figure 3. (a) The $[Hg_2(OTeF_5)_6]^{2-}$ anion in the X-ray crystal structure of $[N(CH_3)_4]_2[Hg_2(OTeF_5)_6]$ showing the immediate coordination environments around Hg_1 and Hg_2 in the structural unit. The F_5Te- groups have been omitted for clarity in panel. (b) Secondary bonding interactions are indicated by dashed lines and thermal ellipsoids are shown at the 50% probability level.

another, but the $Te-O_t-Hg-O_t-Te$ dihedral angles are notably different. The terminal teflate groups of $Hg_{(2)}$ adopt a *gauche*-conformation (dihedral $Te_{(1)}-O_{(1)}-Hg_{(2)}-O_{(6)}-Te_{(6)}$ angle, 34.7(5)°) compared to that observed in solid $Hg(OTeF_5)_2$ (53.7(3)°),[27] whereas the $Hg_{(1)}(OTeF_5)_2$ moiety possesses an *anti*-conformation (dihedral $Te_{(3)}-O_{(3)}-Hg_{(1)}-O_{(4)}-Te_{(4)}$ angle, 122.3(3)°) closer to that calculated for gas-phase $Hg(OTeF_5)_2$ (dihedral $Te-O_t-Hg-O_t-Te$ angle, 139.1°). As expected, the $Te-O_\mu$ bonds (1.788(4) and 1.800(4) Å) are shorter than the $Te-O_t$ bonds (1.811(4), 1.817(4), 1.821(4) Å), consistent with the $Te-O_\mu$ bond having more π character than the $Te-O_t$ bond. Interestingly, the opposite trend is observed in $[Zn(OTeF_5)_2(C_6H_5NO_2)_2]_2$ ($Te-O_\mu$, 1.837(5) Å > $Te-O_t$, 1.782(6) Å).[24] There are no significant differences among the Te–F bond lengths of the F_5TeO- groups, which are comparable to those of $Hg(OTeF_5)_2$[27] and other teflate derivatives.

(d) $Cs_2[Hg(OTeF_5)_4]\cdot Hg(OTeF_5)_2$. The interaction of $Hg(OTeF_5)_2$ with $Cs[OTeF_5]$ affords a chain-type structure (Figure 4 and Figure S5, Supporting Information). The chains result from the interaction of two unique Hg atoms through long Hg---O and Hg---F contacts (vide infra). The chains consist of $Hg(OTeF_5)_2$ molecules that alternate with $[Hg(OTeF_5)_4]^{2-}$ anions along the *c*-axis. Adjacent chains form isolated layers along the *a*- and *b*-axes with no F---F contacts between them that are less than twice the fluorine van der Waals radius (2.94 Å).[42] Columns of Cs^+ cations run parallel to these chains such that each Cs^+ column interacts with three anion chains. The $Cs_{(1)}^+$ cation has nine short Cs---F contacts, six with the $[Hg(OTeF_5)_4]^{2-}$ anions (3.076(1)–3.360(1) Å) and three with the $Hg(OTeF_5)_2$ molecules (3.128(1)–3.347(1) Å).

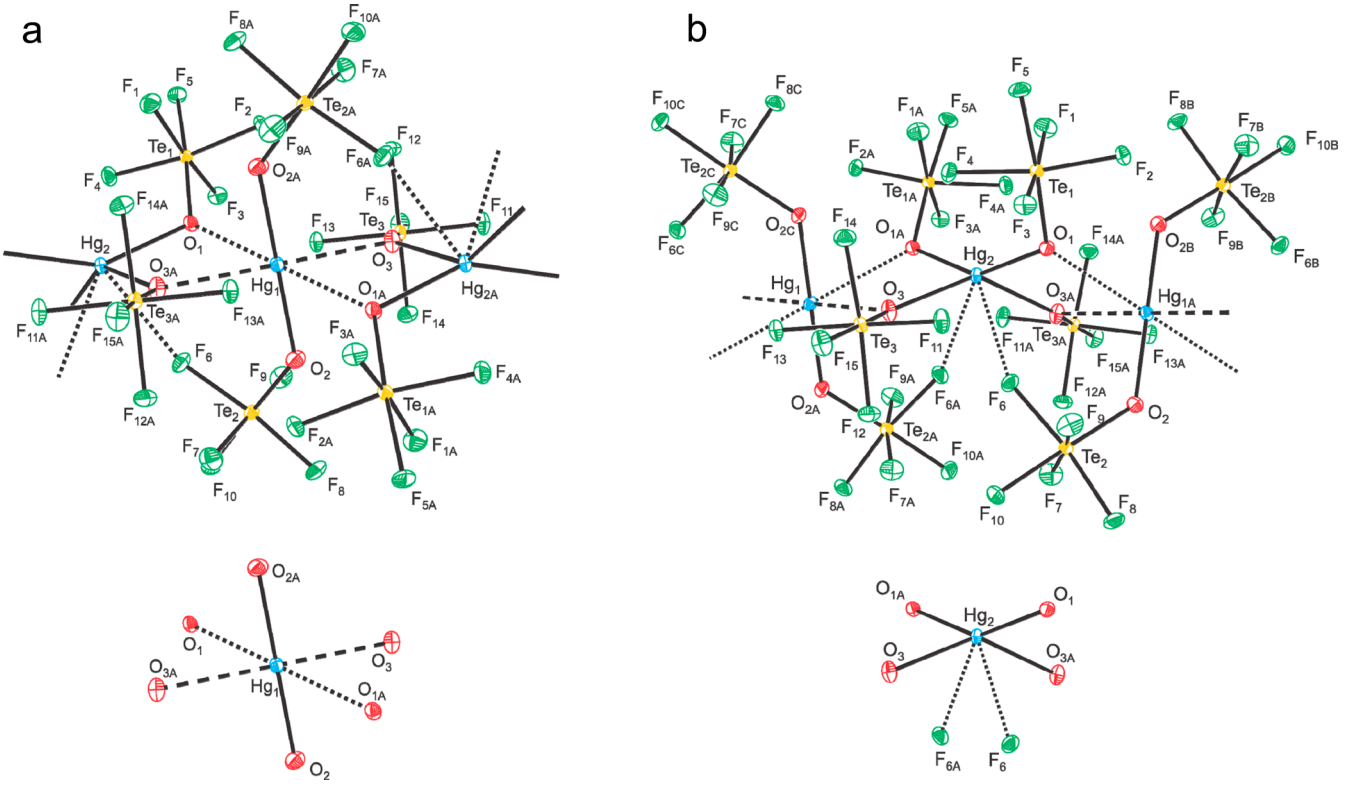

Figure 4. The X-ray crystal structure of $Cs_2[Hg(OTeF_5)_4]\cdot Hg(OTeF_5)_2$ showing the primary coordination sphere (a) of Hg_1 in the "$Hg(OTeF_5)_2$" unit and (b) of Hg_2 in the "$[Hg(OTeF_5)_4]^{2-}$" unit. For clarity, the F_5Te- groups have been omitted in the insets at the bottoms of Figure 4a and Figure 4b. Long contacts are indicated by dashed lines and thermal ellipsoids are shown at the 50% probability level.

DOI: 10.1021/ic502602p
Inorg. Chem. 2015, 54, 1606–1626

The $Hg_{(1)}$ coordination sphere is a distorted pseudo-octahedron with two primary $Hg_{(1)}-O_{(2)}$ bonds (2.058(2) Å), two shorter $Hg_{(1)}\cdots O_{(3)}$ (2.555(1) Å), and two slightly longer $Hg_{(1)}\cdots O_{(1)}$ contacts (2.737(1) Å). The secondary $Hg_{(1)}\cdots O$ contacts involve oxygen atoms from two adjacent $[Hg(OTeF_5)_4]^{2-}$ anions that are significantly less than the sums of the van der Waals radii (3.05 Å for Hg···O),[42] indicating significant covalent interactions between $Hg_{(1)}$ and the oxygen atoms of the $[Hg(OTeF_5)_4]^{2-}$ anions. The oxygen bonding with $Hg_{(1)}$ is reminiscent of that observed for $Hg(OTeF_5)_2$, which also possesses a distorted octahedral coordination sphere consisting of primary Hg−O bonds (2 × 2.016(6) Å) and long $Hg_1\cdots O_2$ (2 × 2.641(7) Å) and Hg···F (2 × 2.810(7) Å) contacts.[27] The $Hg_{(1)}-O_{(2)}$ bonds are slightly longer than in $Hg(OTeF_5)_2$. The corresponding $Te_{(2)}-O_{(2)}$ (1.808(2) Å) and $Te_{(2)}-F$ ($Te-F_a$, 1.838(1)−1.863(1) Å and $Te-F_e$, 1.843(1)−1.856(1) Å) bonds are shortened and elongated with respect to those in $Hg(OTeF_5)_2$ (Te−O, 1.842(7) Å; $Te-F_a$, 1.819(6); and $Te-F_e$, 1.824(6)−1.839(6) Å).[27] The Te−F bond elongations and Te−O bond contractions are consistent with the occurrence of interactions between the $[Hg(OTeF_5)_4]^{2-}$ anions and neutral $Hg_{(1)}(OTeF_5)_2$ units (vide infra), contrasting with the interactions among $Hg(OTeF_5)_2$ molecules in the crystal structure of $Hg(OTeF_5)_2$. The symmetry-imposed *trans-anti*-conformation observed for the $Hg(OTeF_5)_2$ units (dihedral $Te_{(2)}-O_{(2)}-Hg_{(1)}-O_{(2A)}-Te_{(2A)}$ angle, 180°) contrasts with the symmetry-imposed *trans-gauche*-conformation in the crystal structure of $Hg(OTeF_5)_2$ (dihedral Te−O−Hg−O−Te angle, 53.7(3)°), which was attributed to crystal packing.[27] However, the *trans-anti*-conformation is in accordance with that calculated for gas-phase $Hg(OTeF_5)_2$. The $O_{(2)}-Hg_{(1)}-O_{(2A)}$ bond angle (180°) is imposed by symmetry, whereas it is bent in the crystal structure of $Hg(OTeF_5)_2$ ($O_{(1)}-Hg_{(1)}-O_{(1B)}$, 170.5(4)°).[27]

A second mercury environment ($Hg_{(2)}$, Figure 4) has a coordination sphere consisting of two $Hg_{(2)}-O_{(1,1A)}$ (2.186(1) Å), two $Hg_{(2}-O_{(3,3A)}$ (2.287(1) Å) primary bonds, and two long $Hg_{(2)}\cdots F_{(6,6A)}$ contacts (2.731(1) Å). The Hg···F contacts are significantly less than the sum of the mercury and fluorine van der Waals radii (3.02 Å)[42] and are indicative of significant covalent bonding interactions between $Hg_{(2)}$ and the $F_{(6)}$ and $F_{(6A)}$ atoms. The latter belong to two symmetry-related $Hg_{(1,1A)}(OTeF_5)_2$ groups. The $Hg_{(2)}$−O bonds form a flattened tetrahedron having $O-Hg_{(2)}-O$ angles that are larger ($O_{(3A)}-Hg_{(2)}-O_{(3)}$, 137.9(1)° and $O_{(1)}-Hg_{(2)}-O_{(1A)}$, 147.8(1)°) and smaller ($O_{(1)}-Hg_{(2)}-O_{(3A)}$, 81.4(1)°) than the ideal tetrahedral angle (109.5°), whereas the $O_{(1)}-Hg_{(2)}-O_{(3)}$ angle (110.4(1)°) is very close to the ideal angle. Flattening of the tetrahedron results from additional $Hg_{(2)}\cdots F_{(6,6A)}$ contacts. A twist occurs between the $O_{(3A)}Hg_{(2)}O_{(3)}$ and $O_{(1)}Hg_{(2)}O_{(1A)}$ planes, introducing a spiral along the backbone of the chain. The $Hg_{(2)}$−O bonds (2.186(1) and 2.287(1) Å) of $[Hg(OTeF_5)_4]^{2-}$ are comparable to those in $[N(CH_2CH_3)_4]_2[Hg(OTeF_5)_4]$ (2.146(7)−2.275(7) Å) and are longer than the $Hg_{(1)}$−O bonds (2.058(2) Å) of $Hg_{(1)}(OTeF_5)_2$. The Te−O (1.798(1) and 1.816(1) Å), $Te-F_{ax}$ (1.842(1) and 1.843(1) Å), and $Te-F_{eq}$ (1.841(1)−1.863(1) Å) bond lengths are comparable to those of $[N(CH_2CH_3)_4]_2[Hg(OTeF_5)_4]$ (vide supra).

(e) $\{Cs_3[Hg_2(OTeF_5)_7]\cdot Hg(OTeF_5)_2\}\cdot 4SO_2ClF$. The co-crystallization of SO_2ClF afforded another chain structure that is comprised of three crystallographically distinct Hg environments interacting through long Hg···O and Hg···F contacts (vide infra). The chain consists of $Hg(OTeF_5)_2$ molecules that alternate with $[Hg_2(OTeF_5)_7]^{3-}$ anions along the *c*-axis (Figure 5 and Figure S6, Supporting Information). The Cs^+ cations and SO_2ClF molecules

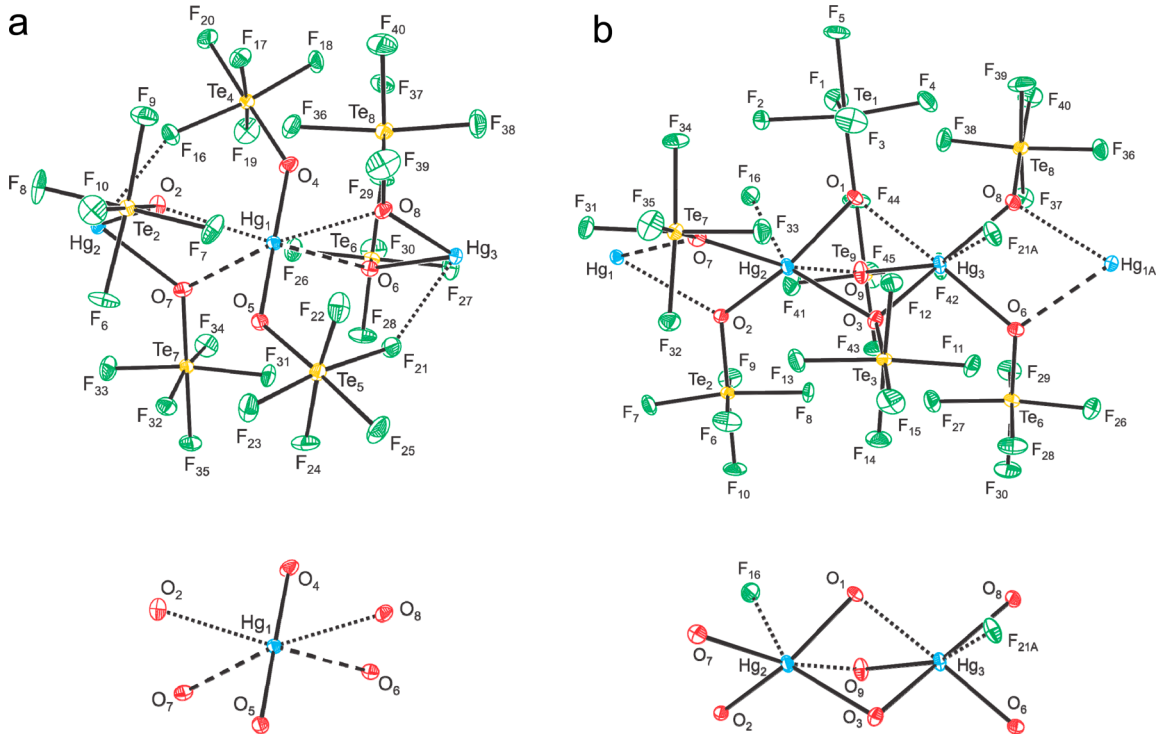

Figure 5. The X-ray crystal structure of $\{Cs_3[Hg_2(OTeF_5)_7]\cdot Hg(OTeF_5)_2\}\cdot 4SO_2ClF$ showing the primary coordination sphere of Hg_1 in the "$Hg(OTeF_5)_2$" unit and (b) of Hg_2 and Hg_3 in the $[Hg_2(OTeF_5)_7]^{3-}$ unit in the anion chain structure. For clarity, the F_5Te- groups have been omitted in the insets at the bottoms of Figure 5a and Figure 5b. Long contacts are indicated by dashed lines, and thermal ellipsoids are shown at the 50% probability level.

DOI: 10.1021/ic502602p
Inorg. Chem. 2015, 54, 1606−1626

form columns that run parallel to the chains. The chains and the SO_2ClF columns stack and alternate along the *a*- and *b*-axes, forming layers; one chain alternates with two SO_2ClF columns (Figure S6, Supporting Information). The SO_2ClF molecules weakly interact with each other and with the $[Hg_2(OTeF_5)_7]^{3-}$ anions through long Cl---F and F---F contacts (Table S5, Supporting Information). Columns of Cs^+ cations stack between the described layers. Each Cs^+ cation has eight short contacts with the $Hg(OTeF_5)_2$ molecules, $[Hg_2(OTeF_5)_7]^{3-}$ anions, and SO_2ClF molecules (Table S5, Supporting Information).

The $Hg_{(1)}$ environment of $\{Cs_3[Hg_2(OTeF_5)_7]\cdot Hg(OTeF_5)_2\}\cdot 4SO_2ClF$ is similar to the $Hg_{(1)}$ environment of $Cs_2[Hg(OTeF_5)_4]\cdot Hg(OTeF_5)_2$, with two primary $Hg_{(1)}$–O bonds ($O_{(4)}$, 2.059(5) Å; $O_{(5)}$, 2.059(5) Å), two shorter $Hg_{(1)}$---O contacts ($O_{(7)}$, 2.529(5) Å; $O_{(6)}$, 2.605(5) Å), and two slightly longer $Hg_{(1)}$---O contacts ($O_{(8)}$, 2.653(5) Å; $O_{(2)}$, 2.737(5) Å). The $O_{(4)}$–$Hg_{(1)}$–$O_{(5)}$ bond angle (174.7(2)°) is intermediate with respect to that calculated for gas-phase $Hg(OTeF_5)_2$ (180°) and that determined in the solid state for $Hg(OTeF_5)_2$ (170.5(4)°). A *trans-anti*-conformation similar to that observed in $Cs_2[Hg(OTeF_5)_4]\cdot Hg(OTeF_5)_2$ is observed, with a dihedral $Te_{(4)}$–$O_{(4)}$–$Hg_{(1)}$–$O_{(5)}$–$Te_{(5)}$ angle of 150.9(4)° that is comparable to that calculated for gas-phase $Hg(OTeF_5)_2$ (139.1°).[27]

The $Hg_{(2)}$ and $Hg_{(3)}$ atoms have coordination spheres similar to that of $Hg_{(2)}$ in $Cs_2[Hg(OTeF_5)_4]\cdot Hg(OTeF_5)_2$, with two groups of $Hg_{(2)}$–O (2.156(5) and 2.169(5) Å; 2.356(5) and 2.359(5) Å) and $Hg_{(3)}$–O (2.211(5) and 2.234(5) Å; 2.266(5) and 2.369(5) Å) bonds. The $F_5TeO_{(3)}$– group, which is equally shared between $Hg_{(2)}$ and $Hg_{(3)}$ ($Hg_{(2)}$–$O_{(3)}$, 2.356(5) Å; $Hg_{(3)}$–$O_{(3)}$, 2.369(5) Å), is best described as a bridging F_5TeO_μ– group. The $Hg_{(2)}$ and $Hg_{(3)}$ atoms are also asymmetrically linked to each other through long Hg---O contacts ($Hg_{(2)}$–$O_{(9)}$, 2.680(5) Å and $Hg_{(3)}$–$O_{(1)}$, 2.631(5) Å) and to the $Hg_{(1)}$ atom through long Hg---F contacts ($Hg_{(2)}$–$F_{(16)}$, 2.668(5) Å and $Hg_{(3)}$–$F_{(21A)}$, 2.675(5) Å). The four short Hg–O bonds form distorted tetrahedral environments around $Hg_{(2)}$ and $Hg_{(3)}$ having large O–Hg–O bond angles ($Hg_{(2)}$, 130.8(2) and 156.4(2)°; $Hg_{(3)}$, 127.2(2) and 149.2(2)°) similar to those observed in $Cs_2[Hg(OTeF_5)_4]\cdot Hg(OTeF_5)_2$ (see above). The Te–O and Te–F bond lengths are also comparable to those in $Cs_2[Hg(OTeF_5)_4]\cdot Hg(OTeF_5)_2$.

Raman Spectroscopy. The low-temperature solid-state Raman spectra of $[N(CH_2CH_3)_4]_2[Hg(OTeF_5)_4]$, $[N(CH_3)_4]_3[Hg(OTeF_5)_5]$, $[N(CH_3)_4][Hg_2(OTeF_5)_6]$, and $Cs_2[Hg(OTeF_5)_4]\cdot Hg(OTeF_5)_2$ are shown in Figures 6–9 and Figures S7–S9 of the Supporting Information. Vibrational frequencies and mode descriptions are listed in abbreviated form in Tables 7–10, and detailed mode descriptions, which account for vibrational coupling, are provided in Tables S7–S10 of the Supporting Information. Spectral assignments were made by comparison with the calculated frequencies and Raman intensities obtained for the energy-minimized gas-phase geometries of the $[Hg(OTeF_5)_4]^{2-}$ (S_4), $[Hg(OTeF_5)_5]^{3-}$ (C_1), and $[OTeF_5]^-$ (C_{4v}) anions, and the presently unknown $[Hg_2(OTeF_5)_6]^{2-}$ (D_2), and $[Hg_3(OTeF_5)_8]^{2-}$ (C_1) anions. The vibrational assignments were also aided by comparison with the recently published experimental and calculated frequencies of $Hg(OTeF_5)_2$.[27] The low-temperature Raman spectra of $[N(CH_2CH_3)_4][OTeF_5]$, $[N(CH_3)_4][OTeF_5]$, and $Cs[OTeF_5]$ were also recorded for comparison with mode assignments for the F_5TeO– ligands (Table S11 and Figure S10, Supporting Information). The vibrational bands of the $[N(CH_3)_4]^+$[47] and

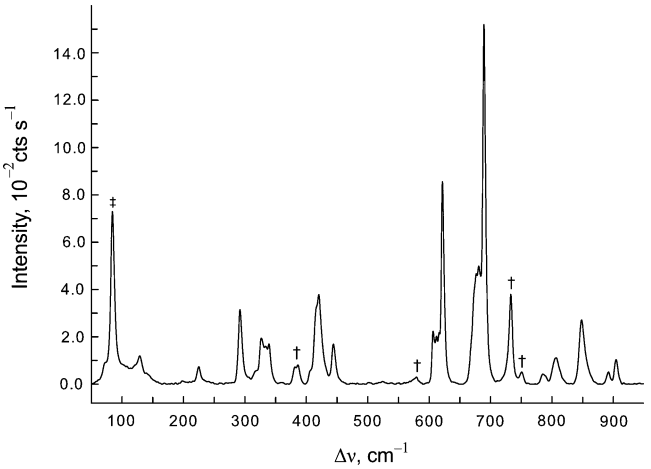

Figure 6. Raman spectrum of $[N(CH_2CH_3)_4]_2[Hg(OTeF_5)_4]$ recorded at −155 °C using 1064-nm excitation. The full spectrum, including the cation bands, is shown in Figure S7 of the Supporting Information. Symbols denote FEP (†) bands and an instrumental artifact (‡).

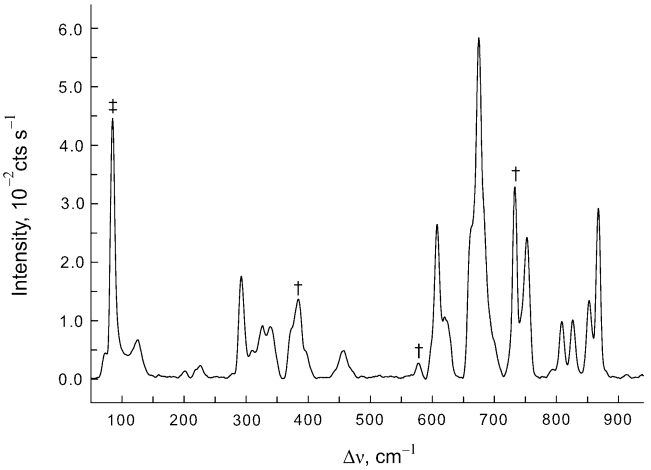

Figure 7. Raman spectrum of $[N(CH_3)_4]_3[Hg(OTeF_5)_5]$ recorded at −155 °C using 1064-nm excitation. The full spectrum, including the cation bands, is shown in Figure S8 of the Supporting Information. Symbols denote FEP (†) bands and an instrumental artifact (‡).

$[N(CH_2CH_3)_4]^+$[48,49] cations have been previously assigned and are not discussed in the ensuing section.

(a) $[N(CH_2CH_3)_4]_2[Hg(OTeF_5)_4]$ and $[N(CH_3)_4]_3[Hg(OTeF_5)_5]$. Values in square brackets refer to the $[Hg(OTeF_5)_5]^{3-}$ anion. Overall, the trends in vibrational frequencies and intensities for the calculated $[Hg(OTeF_5)_4]^{2-}$ and $[Hg(OTeF_5)_5]^{3-}$ anions agree well with the experimental values. In the case of $[Hg(OTeF_5)_4]^{2-}$, the "asymmetric" $[\nu(Hg{-}O) - \nu(Te{-}O)]$-type stretching modes were overestimated by 31–32 cm^{-1}, whereas the "symmetric" $[\nu(Hg{-}O) + \nu(Te{-}O)]$-type stretching modes were underestimated by 18–30 cm^{-1}. In the case of $[Hg(OTeF_5)_5]^{3-}$, the "asymmetric"-type modes were overestimated by 23–26 cm^{-1}, whereas the "symmetric"-type modes were in good agreement with the experimental values.

The $\nu(Hg{-}O)$ and $\nu(Te{-}O)$ anion stretches couple, but to a lesser extent than in $Hg(OTeF_5)_2$. Four [five] modes are derived from coupled "asymmetric" $[\nu(Hg{-}O) - \nu(Te{-}O)]$-type stretches. The totally in-phase coupled mode (calcd, 880 [893] cm^{-1}) was observed at 848 [867] cm^{-1}, and the two [four] out-of-phase coupled modes (calcd, 839/839 [832/849/872/877] cm^{-1}) appear as one [three] band(s) (exptl, 807 [809/827/853] cm^{-1}).

DOI: 10.1021/ic502602p
Inorg. Chem. 2015, 54, 1606–1626

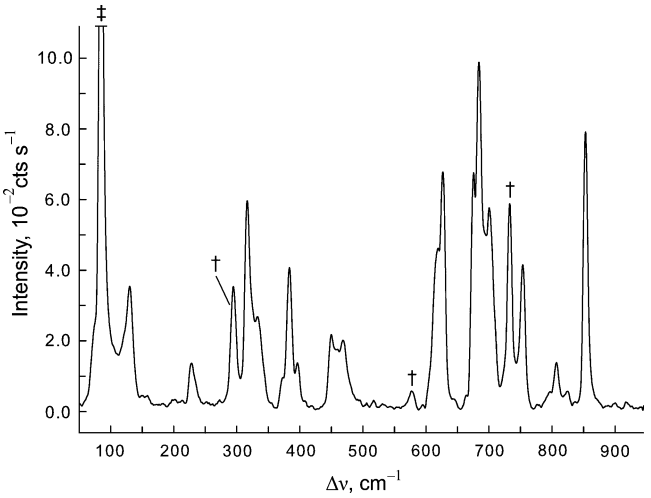

Figure 8. Raman spectrum of $[N(CH_3)_4]_2[Hg_2(OTeF_5)_6]$ recorded at −155 °C using 1064-nm excitation. The full spectrum, including the cation bands, is shown in Figure S9 of the Supporting Information. Symbols denote FEP (†) bands and an instrumental artifact (‡).

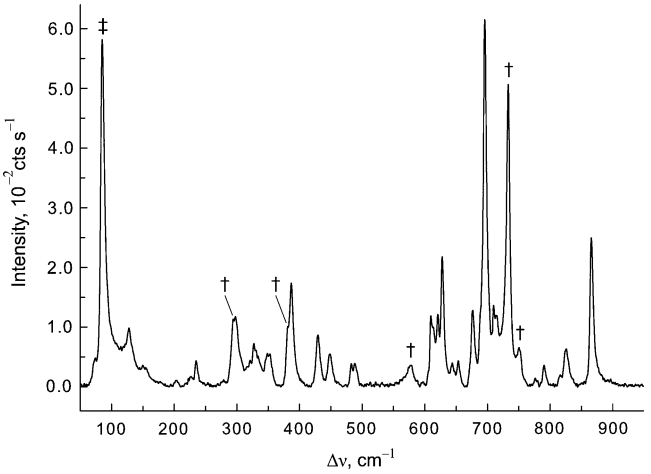

Figure 9. Raman spectrum of $Cs_2[Hg(OTeF_5)_4]\cdot Hg(OTeF_5)_2$ recorded at −155 °C using 1064-nm excitation. Symbols denote FEP (†) bands and an instrumental artifact (‡).

In each case, the experimental in-phase and out-of-phase coupled modes are shifted to higher frequency relative to the corresponding modes in $Hg(OTeF_5)_2$ (825 and 801 cm^{-1}, respectively);[27] the high-frequency shifts are also reproduced by their calculated vibrational frequencies ($Hg(OTeF_5)_2$, 824 and 787/793 cm^{-1}, respectively).

The totally in-phase coupled modes, 848 [867] cm^{-1}, occur at frequencies that approach those of the ν(Te−O) stretches of the $[OTeF_5]^-$ anion ($[N(CH_2CH_3)_4]^+$ salt, 866 cm^{-1}; $[N(CH_3)_4]^+$ salt, 854 cm^{-1}; Table S11, Supporting Information). This suggests that the major contributors to these coupled modes are the ν(Te−O) stretches. The Hg−O bonds are somewhat elongated when compared with those of $Hg(OTeF_5)_2$ as a result of the 2− and 3− anion charges. Accordingly, the Te−O bonds are somewhat shorter (see X-ray Crystallography), having acquired more π character resulting in the observed and calculated high-frequency shifts of the "asymmetric" [ν(Hg−O) − ν(Te−O)]-type stretches.

The three [two] modes associated with the coupled "symmetric" [ν(Hg−O) + ν(Te−O)]-type stretching modes of

Table 7. Experimental Raman Frequencies and Intensities for $[Hg(OTeF_5)_4]^{2-}$ in $[N(CH_2CH_3)_4]_2[Hg(OTeF_5)_4]$ and Calculated Vibrational Frequencies and Intensities for $[Hg(OTeF_5)_4]^{2-}$

exptl $[Hg(OTeF_5)_4]^{2-}$ in $[N(CH_2CH_3)_4]_2[Hg(OTeF_5)_4]$[a,b]	calcd $[Hg(OTeF_5)_4]^{2-}$ (S_4) [a,c,d,e,f]		
			assgnts
848(18)	879(98)[0]	A	
807(7)	839(36)[375]	E	ν(Hg-O) – ν(Te-O)
	839(27)[439]	B	
681(33)	683(2)[372]	B	Te-F_e stretches
	681(2)[404]	E	
	679(5)[0]	A	
677(31)	677(6)[59]	B	
	675(19)[0]	A	
	673(<1)[17]	E	
689(100)	660(117)[0]	A	ν(Te-F_a) + ν(TeF_{4e})$_{small}$
	656(5)[122]	E	
	656(5)[132]	B	
622(57)	609(5)[<0.1]	B	Te-F_e stretches
	608(2)[2]	E	
616(14)	608(4)[0]	A	
612(13)	604(14)[0]	A	ν(Te-F_a) – ν(TeF_{4e})
606(14)	600(2)[<1]	B	
	599(1)[6]	E	
420(25)[f]	390(<1)[90]	E	ν(Hg-O) + ν(Te-O)
417, sh	390(3)[7]	B	
406, sh	388(4)[0]	A	
339(11)	340(<1)[0]	A	δ(TeF_{4e})$_{umb}$
	338(<1)[75]	B	δ(F-Te-F)
	338(2)[0]	A	
334(11)	337(<1)[14]	E	
	335(<1)[20]	B	
327(13)	334(<1)[58]	E	
	332(<0.1)[0]	A	
	329(3)[65]	B	δ(TeF_{4e})$_{umb}$
	328(<1)[90]	E	
317, sh, br	320(1)[109]	B	δ(O-Hg-O)$_{o.o.p.}$
	318(4)[0]	A	
	313(<1)[25]	E	ρ_t(O-Hg-O)
292(15)	286(2)[<0.1]	B	δ(F-Te-F)
	286(2)[<0.1]	E	
	286(<0.1)[0]	A	
225(5)	216(1)[0]	A	ρ_w(F-Te-F)
	215(<0.1)[<1]	B	
	214(<0.1)[<1]	E	
	213(<1)[0]	A	
	211(<1)[7]	E	ρ_w(F-Te-F) / ρ_w(F-Te-O)
	211(<1)[5]	B	ρ_w(F-Te-F)
129(8)	113(2)[0]	A	ρ_t($F_aF_{4e}Te$)

[a]Frequencies are given in cm^{-1}. [b]Values in parentheses denote relative Raman intensities. The Raman spectrum was recorded in an FEP sample tube at −150 °C using 1064 nm excitation. The abbreviations denote shoulder (sh), broad (br), and not observed (n.o.). [c]Values in parentheses denote calculated Raman intensities ($Å^4$ amu^{-1}), whereas values in square brackets denote calculated infrared intensities (km mol^{-1}). Assignments are for the energy-minimized geometry calculated at the PBE1PBE/def2-TZVPP level; only general descriptions of the vibrational modes are listed. The abbreviations denote umbrella (umb), equatorial (4e, where the four F_e atoms are in-phase), axial (a), stretch (ν), bend (δ), twist (ρ_t), wag (ρ_w), and rock (ρ_r). [d]See Table S7 of the Supporting Information for a complete listing of frequencies and detailed descriptions of the assignments. [e]Calculated band intensity corresponds to one component of the doubly degenerate E mode. [f]Overlaps with a cation band.

$[Hg(OTeF_5)_4]^{2-}$ and $[Hg(OTeF_5)_5]^{3-}$ (calcd, 388/390/390 [401/428] cm^{-1}) were observed as three [one] bands at 406/417/420 [396] cm^{-1}. In contrast to their "asymmetric" counterparts, these bands are shifted to lower frequencies relative to the corresponding $Hg(OTeF_5)_2$ bands (exptl, 472/481/511 cm^{-1};

DOI: 10.1021/ic502602p
Inorg. Chem. 2015, 54, 1606−1626

calcd, 506/516/528/530). The greater low-frequency shift observed for $[Hg(OTeF_5)_5]^{3-}$ relative to that of $[Hg(OTeF_5)_4]^{2-}$ is consistent with its higher negative charge and more ionic Hg−O bonds. The observed low-frequency shifts suggest that the ν(Hg−O) stretches are significant contributors to the coupled "symmetric" [ν(Hg−O) + ν(Te−O)]-type stretching modes.

The bands between 689 [690] and 606 [578] cm^{-1} are assigned to ν(Te−F) stretches, which are shifted to lower frequency relative to those of $Hg(OTeF_5)_2$ (735−624 cm^{-1}),[27] in accordance with the Te−F bond lengths being slightly longer in both anions than in $Hg(OTeF_5)_2$ (see X-ray Crystallography). These shifts are well reproduced by the calculations ($[Hg(OTeF_5)_4]^{2-}$, 683−599 cm^{-1}; $[Hg(OTeF_5)_5]^{3-}$, 688−568 cm^{-1}; $Hg(OTeF_5)_2$, 726−640 cm^{-1}). The in-phase coupled axial ν_s(Te−F$_a$) modes are the most intense bands in both Raman spectra ($[Hg(OTeF_5)_4]^{2-}$, 689 cm^{-1}; $[Hg(OTeF_5)_5]^{3-}$, 675 cm^{-1}) as was observed for $Hg(OTeF_5)_2$ (709 cm^{-1}). The ν_s(Te−F$_a$) stretches occur at higher frequencies than those of their respective $[OTeF_5]^-$ salts ($[N(CH_2CH_3)_4]^+$, 643−579 cm^{-1}; $[N(CH_3)_4]^+$, 650−590 cm^{-1}; Table S11, Supporting Information), which is presumably the result of smaller negative charges on the F$_5$TeO− groups of the mercury teflate anions (see Computational Results and NBO sections).

The band at 317 [316] cm^{-1} is assigned to the O−Hg−O bending mode, by analogy with the weak band observed at 331 cm^{-1} in $Hg(OTeF_5)_2$ (calcd; $[Hg(OTeF_5)_4]^{2-}$, 313−320; $[Hg(OTeF_5)_5]^{3-}$, 316-319; $Hg(OTeF_5)_2$, 332 cm^{-1}).

(b) $[N(CH_3)_4][Hg_2(OTeF_5)_6]$. Overall, the vibrational frequency and intensity trends for the calculated gas-phase $[Hg_2(OTeF_5)_6]^{2-}$ anion are in very good agreement with the experimental trends for $[N(CH_3)_4][Hg_2(OTeF_5)_6]$. Discrepancies between the calculated and experimental frequencies may arise from failure to reproduce the *anti*- and *gauche*-conformations observed around Hg$_{(1)}$ and Hg$_{(2)}$ in the solid state (see Computational Results).

The atomic displacements of the gas-phase anion indicate that the highest frequency bands (805−853 cm^{-1}) of $[Hg_2(OTeF_5)_6]^{2-}$ are derived from "asymmetric" [ν(Hg−O) − ν(Te−O)]-type stretching modes. The intense band at 853 cm^{-1} (calcd, 856 cm^{-1}) is assigned to the totally in-phase coupled mode, [ν(Hg−O$_\mu$) − ν(Te−O$_\mu$)] + [ν(Hg−O$_t$) − ν(Te−O$_t$)]. The latter frequency is comparable to that observed for the corresponding mode in $[Hg(OTeF_5)_4]^{2-}$ (848 cm^{-1}) and the ν(Te−O) stretch of the $[OTeF_5]^-$ anion in its $[N(CH_3)_4]^+$ salt (854 cm^{-1}). The broad band at 826 cm^{-1} is assigned to an out-of-phase [ν(Hg−O$_t$) − ν(Te−O$_t$)]-type stretch (calcd, 822 cm^{-1}). The calculated frequencies, 819 and 823 cm^{-1}, are predicted to be weak in the Raman spectrum and were not observed. These frequencies are essentially the same as that of the corresponding mode in $Hg(OTeF_5)_2$ (exptl, 825 cm^{-1}; calcd, 824 cm^{-1}). The bands at 805 and 808 cm^{-1} are assigned to an out-of-phase mode involving both the bridging and terminal teflate groups (calcd, 806 cm^{-1}). The frequencies are comparable to that observed for the corresponding mode in $[Hg(OTeF_5)_4]^{2-}$ (exptl, 807 cm^{-1}; calcd, 839/839/839 cm^{-1}) and $Hg(OTeF_5)_2$ (exptl, 801 cm^{-1}; calcd, 787/793 cm^{-1}). An additional low-intensity, out-of-phase [ν(Hg−O$_\mu$) − ν(Te−O$_\mu$)]-type stretching band was calculated (812 cm^{-1}), but was too weak to be observed.

The bands at 470 and 479 cm^{-1} in the Raman spectrum of $[Hg_2(OTeF_5)_6]^{2-}$ are associated with the "symmetric" in-phase coupled [ν(Hg−O$_t$) + ν(Te−O$_t$)]-type stretching mode (calcd, 463 cm^{-1}). The out-of-phase coupled counterparts (calcd, 464/469/465 cm^{-1}) are predicted to be weak and were not observed. The bands at 470 and 479 cm^{-1} are reminiscent of the corresponding bands in $Hg(OTeF_5)_2$ (exptl, 472/481/511 cm^{-1}; calcd, 504 cm^{-1}). The band at 397 cm^{-1} was assigned to a mode involving only ν(Hg−O$_\mu$) stretches, [ν(Hg$_1$−O$_{24}$) + ν(Hg$_2$−O$_{34}$)] − [ν(Hg$_2$−O$_{24}$) + ν(Hg$_1$−O$_{34}$)]. The experimental frequency is in excellent agreement with the calculated value (392 cm^{-1}). A similar weak band is predicted at 407 cm^{-1} for [ν(Hg$_1$−O$_{24}$) + ν(Hg$_1$−O$_{34}$)] − [ν(Hg$_2$−O$_{24}$) + ν(Hg$_2$−O$_{34}$)] but was not observed. The experimental frequencies suggest that the terminal teflate groups of $[Hg_2(OTeF_5)_6]^{2-}$ are similar to those of $Hg(OTeF_5)_2$ and that the negative charge mainly resides on the bridging teflate groups, resulting in Hg−O$_\mu$ bonds that are overall more ionic and Te−O$_\mu$ bonds with greater π character (see Computational Results and NBO sections).

The band at 316 cm^{-1} (calcd, 316/320 cm^{-1}) is tentatively assigned to O−Hg−O bending modes by analogy with those observed and calculated for $[Hg(OTeF_5)_4]^{2-}$ (exptl, 317 cm^{-1}; calcd, 318/320 cm^{-1}) and $Hg(OTeF_5)_2$ (exptl, 331 cm^{-1}; calcd, 332 cm^{-1}).

The bands between 604 and 707 cm^{-1} (calcd, 609−699 cm^{-1}) are assigned to ν(Te−F) stretches and are intermediate with respect to those observed for $[Hg(OTeF_5)_4]^{2-}$ (exptl, 606−689 cm^{-1}; calcd, 599−683 cm^{-1}) and $Hg(OTeF_5)_2$ (exptl, 624−735 cm^{-1}; calcd, 640−726 cm^{-1}). The bands between 674 and 684 cm^{-1} (calcd, 665−673 cm^{-1}) involve axial ν(Te−F) stretching modes, with the totally symmetric stretching mode at 684 cm^{-1} being the strongest band in the Raman spectrum (calcd, 673 cm^{-1}).

(c) $Cs_2[Hg(OTeF_5)_4]\cdot Hg(OTeF_5)_2$. The use of the calculated frequencies and intensities of the hypothetical $[Hg_3(OTeF_5)_8]^{2-}$ anion (see Computational Results) allowed the assignment of the experimental Raman spectrum of $Cs_2[Hg(OTeF_5)_4]\cdot Hg(OTeF_5)_2$. The approach allowed modes involving only the $[Hg(OTeF_5)_4]^{2-}$ anion or $Hg(OTeF_5)_2$ moieties, as well as coupled modes of the anion and $Hg(OTeF_5)_2$, to be distinguished. There is very good agreement between the experimental and calculated frequencies.

The bands occurring between 776 and 866 cm^{-1} are assigned to "asymmetric" [ν(Hg−O) − ν(Te−O)]-type stretches. The strong band at 866 cm^{-1} (calcd, 853 cm^{-1}) is assigned to the totally in-phase coupled mode. Both $[Hg(OTeF_5)_4]^{2-}$ and $Hg(OTeF_5)_2$ contribute to this mode, which occurs at higher frequency than the analogous mode in $[N(CH_2CH_3)_4]_2[Hg(OTeF_5)_4]$ (848 cm^{-1}). The bands at 776/780/790/795, 816, and 826 cm^{-1} are assigned to out-of-phase coupled modes, by comparison with their calculated frequencies (791/792, 812/814, and 823/826/834, respectively).

The three bands observed at 483, 488, and 492 cm^{-1} (calcd, 487/488, 498/499 cm^{-1}) are assigned to the coupled "symmetric" [ν(Hg−O) + ν(Te−O)]-type stretching modes of the Hg(OTeF$_5$)$_2$ moieties and occur at frequencies similar to the corresponding modes in solid $Hg(OTeF_5)_2$ (exptl, 472/481/511 cm^{-1}; calcd, 506/516/528/530 cm^{-1}).[27] The calculated frequencies at 419/419 and 435/444 cm^{-1} only involve ν(Hg−O) stretches and were observed at 430 and 448 cm^{-1}, respectively.

The bands between 604 and 721 cm^{-1} (calcd, 620−707 cm^{-1}) are assigned to the ν(Te−F) stretching modes of the F$_5$Te-groups and are comparable to those in both $[Hg(OTeF_5)_4]^{2-}$ (exptl, 606−689 cm^{-1}; calcd, 599−683 cm^{-1}) and $Hg(OTeF_5)_2$ (exptl, 624−735 cm^{-1}; calcd, 640−726 cm^{-1}).

Computational Results. The electronic structures of the $[Hg(OTeF_5)_4]^{2-}$ (S_4), $[Hg(OTeF_5)_5]^{3-}$ (C_1), $[OTeF_5]^-$ (C_{4v}), $[Hg_2(OTeF_5)_6]^{2-}$ (D_2), and $[Hg_3(OTeF_5)_8]^{2-}$ (C_1) anions were calculated using PBE1PBE functionals and def2-TZPP basis sets

DOI: 10.1021/ic502602p
Inorg. Chem. 2015, 54, 1606−1626

Table 8. Experimental Raman Frequencies and Intensities for $[Hg(OTeF_5)_5]^{3-}$ in $[N(CH_3)_4]_3[Hg(OTeF_5)_5]$ and Calculated Vibrational Frequencies and Intensities for $[Hg(OTeF_5)_5]^{3-}$

exptl $[Hg(OTeF_5)_5]^{3-}$ in $[N(CH_3)_4]_3[Hg(OTeF_5)_5]$[a,b]	calcd $[Hg(OTeF_5)_5]^{3-}$ (C_1) [a,c,d]	assgnts
867(52)	893(222)[10]	ν(Hg-O) – ν(Te-O)
853(22)	877(54)[315]	
	872(71)[322]	
827(16)	849(4)[528]	
809(16)	832(46)[25]	
	688(<1)[357]	Te-F_e stretches
690, sh	688(<1)[336]	
682, sh	687(3)[22]	
	686(4)[1]	
675(100)	657(112)[13]	ν(Te-F_a) + ν(TeF_{4e})
670, sh	657(<1)[560]	Te-F_e stretches
	655(6)[173]	
	654(2)[125]	
	653(2)[60]	ν(Te-F_e) / ν(Te-F_a) + ν(TeF_{4e})
661(42)	652(10)[10]	Te-F_e stretches
	652(<1)[<1]	
	649(1)[9]	
627(15)	637(74)[16]	ν(Te-F_a) + ν(TeF_{4e})
622(18)	635(7)[152]	
	634(9)[152]	
619(15)	613(3)[3]	Te-F_e stretches
	613(3)[15]	
608(42)	597(1)[19]	ν(Te-F_a) – ν(TeF_{4e})
	597(4)[7]	
	587(4)[<1]	Te-F_e stretches
600. sh	586(5)[1]	
	586(1)[1]	
	570(3)[1]	ν(Te-F_a) – ν(TeF_{4e})
578(3)	569(1)[10]	
	568(2)[8]	
396(7)	428(<1)[60]	ν(Hg-O) + ν(Te-O)
	401(10)[10]	
	344(1)[42]	δ(F-Te-F) / ρ_w(F-Te-F)
	344(1)[35]	
	343(1)[28]	
341(13)	343(1)[13]	
339(13)	343(<1)[53]	
337(13)	342(<1)[2]	
	342(<1)[7]	
	340(<1)[2]	
328(15)	340(<1)[9]	δ(F-Te-F) / δ(F-Te-O)
	338(1)[27]	
	336(1)[96]	δ(F-Te-F) / δ(TeF_{4e})$_{umb}$
326(13)	335(<1)[140]	δ(F-Te-F) / ρ_w(F-Te-F) / δ(TeF_{4e})$_{umb}$
	333(1)[13]	δ(F-Te-F) / ρ_w(F-Te-F)
324(13)	328(<0.1)[1]	δ(TeF_{4e})$_{umb}$
	327(<0.1)[49]	
320(10)	324(3)[121]	δ(F-Te-F) / δ(F-Te-O)
	322(6)[35]	
	319(3)[50]	δ(O-Hg-O)
316(7)	319(1)[83]	
	316(2)[30]	
312(7)	312(<1)[<1]	ρ_t(Hg_1-$O_8O_{12}O_{25}$)
308(7)	311(2)[21]	ρ_w(O-Hg-O)
	303(<1)[12]	ρ_t(Hg_1-$O_{12}O_{22}O_{34}$)
	290(1)[3]	δ(F-Te-F)
	288(1)[2]	
292(15)	281(3)[<0.1]	δ(F-Te-F)
	280(<1)[<1]	
	280(1)[<1]	
n.o.	229(<0.1)[9]	δ(F-Te-F) / ρ_w(F-Te-F)
	219(<1)[<0.1]	ρ_w(F-Te-F)
	218(<0.1)[<0.1]	
	218(<0.1)[<0.1]	
226(4)	217(1)[<1]	ρ_w(F-Te-F) / ρ_w(F-Te-O)
	213(<0.1)[<0.1]	ρ_w(F-Te-F)
	213(<1)[<0.1]	
	198(<0.1)[<0.1]	δ(F-Te-F) / ρ_w(F-Te-O)
	196(<0.1)[<0.1]	
	192(<1)[<1]	
	191(<1)[<1]	
201(3)	189(<0.1)[<1]	
	189(<0.1)[<1]	
	188(<0.1)[<0.1]	
	186(<0.1)[<1]	
n.o.	153(<0.1)[19]	coupled deformation and torsion modes
124(10)	112(2)[<0.1]	

[a]Frequencies are given in cm^{-1}. [b]Values in parentheses denote relative Raman intensities. The Raman spectrum was recorded in an FEP sample tube at −150 °C using 1064-nm excitation. The abbreviations denote shoulder (sh), broad (br), and not observed (n.o.). [c]Values in parentheses denote calculated Raman intensities ($Å^4$ amu^{-1}), whereas values in square brackets denote calculated infrared intensities (km mol^{-1}). Assignments are for the energy-minimized geometry calculated at the PBE1PBE/def2-TZVPP level; only general descriptions of the vibrational modes are listed. The abbreviations denote umbrella (umb), equatorial (4e, where the four F_e atoms are in-phase), axial (a), stretch (ν), bend (δ), twist (ρ_t), wag (ρ_w), and rock (ρ_r). [d]See Table S8 of the Supporting Information for a complete listing of frequencies and detailed descriptions of the assignments.

starting from the crystallographic coordinates (C_1 symmetry). The PBE1PBE/def2-TZPP method was previously shown to be reliable for related systems, i.e., $Hg(OTeF_5)_2$ and $[Hg(OTeF_5)_2]_3{\cdot}2NgF_2$ (Ng = Kr, Xe).[27] All calculations resulted in stationary points with all frequencies real. Calculated vibrational frequencies, intensities, and geometrical parameters are reported in Tables 2−5 and 7−10 and Tables S7−S16 of the Supporting Information and energy-minimized structures are shown in Figure 10 and Figure S10 of the Supporting Information. NBO analyses for all species were carried out with NBO 6.0[50] at the same level of theory (Tables S17−S21, Supporting Information).

Calculated Geometries. *(a) $[Hg(OTeF_5)_4]^{2-}$.* The $[Hg(OTeF_5)_4]^{2-}$ anion was optimized to S_4 symmetry, giving a local Hg(II) environment that is close to tetrahedral (∠O−Hg−O: 4 × 108.0° and 2 × 112.4°), in contrast with the more distorted tetrahedral environment observed in the solid state (∠O−Hg−O: 86.3(2)−125.9(3)°) (Figure 1). This strongly suggests that the solid-state distortion is likely the result of crystal packing, i.e., weak anion−cation interactions. The calculated Hg−O (2.226 Å) and Te−O (1.799 Å) bond lengths are in very good agreement with the experimental values (2.216(7) and 1.797(6) Å, respectively) and are elongated and shortened in comparison to those calculated for $Hg(OTeF_5)_2$ (2.008 and 1.865 Å, respectively),[27] in agreement with the observed trend. The calculated Te−F_{ax} and Te−F_{eq} bond lengths (1.864−1.871 Å) are, on average, slightly longer when compared with the experimental bond lengths (1.816(6)−1.861(6) Å), and the calculated Hg−O−Te angles (132.4°) are somewhat more open than the experimental angles (118.2(3)−124.1(3)°) It is noteworthy that the geometries of the related $C(OTeF_5)_4$ molecule and $[B(OTeF_5)_4]^-$ anion also optimized to S_4 symmetry[30] and that the calculated O−Hg−O angles are almost equal to those of $C(OTeF_5)_4$ (∠O−C−O: 4 × 107.8° and 2 × 113.0°), whereas the O−B−O angles are equal to the ideal tetrahedral angle (∠O−B−O: 4 × 109.4° and 2 × 109.5°).

(b) $[Hg(OTeF_5)_5]^{3-}$. The $[Hg(OTeF_5)_5]^{3-}$ anion optimized to a slightly distorted trigonal bipyramidal environment around Hg(II) (τ = 0.905),[46] contrasting with the distorted square pyramidal geometries observed in the solid state (Figure 2 and Figure S2, Supporting Information). Attempts to optimize the square pyramidal structure resulted in the more energetically favorable trigonal bipyramidal geometry, confirming the influence of the cation−anion interactions on the solid-state geometry (see X-ray Crystallography). In the gas phase, the axial Hg−O_{ax} bond lengths (2.110 and 2.111 Å) are significantly shorter than the equatorial Hg−O_{eq} bond lengths (2.481, 2.482, 2.510 Å). Although more pronounced in the gas-phase calculation, these bond length differences are also present in the solid state, with two shorter Hg−O bonds ($[N(CH_3)_4]^+$ salt: 2.227(5)

DOI: 10.1021/ic502602p
Inorg. Chem. 2015, 54, 1606−1626

Table 9. Experimental Raman Frequencies and Intensities for $[Hg_2(OTeF_5)_6]^{2-}$ in $[N(CH_3)_4]_2[Hg_2(OTeF_5)_6]$ and Calculated Vibrational Frequencies and Intensities for $[Hg_2(OTeF_5)_6]^{2-}$

exptl $[Hg_2(OTeF_5)_6]^{2-}$ in $[N(CH_3)_4]_2[Hg_2(OTeF_5)_6]$[a,b]	calcd $[Hg_2(OTeF_5)_6]^{2-}$ (D_2)[a,c,d]		
			assgnts
853(77)	856(127)[0]	A	ν(Hg-O) – ν(Te-O)
826(5), br	823(<1)[665]	B_2	
	822(47)[6]	B_1	
	819(<1)[593]	B_3	
808(12)	812(<0.1)[543]	B_1	
805(12), br	806(18)[0]	A	
707(30)	699(1)[138]	B_3	Te-F_e stretches
	699(21)[0]	A	
	698(4)[164]	B_2	
	698(<0.1)[525]	B_1	
703(52)	696(1)[539]	B_2	
699(47)	695(5)[17]	B_3	
689(49)	691(3)[0]	A	
	689(3)[5]	B_1	
	688(<0.1)[59]	B_2	
	687(<0.1)[1]	B_3	
	679(<0.1)[216]	B_3	
	675(2)[2]	B_2	
684(100)	673(155)[0]	A	ν(Te-F_a) + ν(TeF_{4e})
678(51)	670(<1)[309]	B_3	ν(Te-F_a)
674(62)	669(<0.1)[51]	B_2	
	669(11)[3]	B_1	
	666(15)[0]	A	ν(Te-F_a) + ν(TeF_{4e})
	665(<0.1)[136]	B_1	
627(72)	624(<1)[<1]	B_1	ν(Te-F_e) / ν(Te-F_a)
621(41)	623(2)[<1]	B_2	
618(41)	622(17)[0]	A	
613(34)	621(4)[2]	B_3	
604(12)	621(12)[0]	A	
	619(<1)[5]	B_3	
	617(5)[0]	A	
	617(<0.1)[<0.1]	B_1	
	617(<0.1)[<1]	B_2	
	616(<1)[<1]	B_1	
	610(2)[0]	A	
	609(<0.1)[<1]	B_1	
479(8)	469(<0.1)[116]	B_2	ν(Hg-O) + ν(Te-O)
470(17)	465(<0.1)[<1]	B_1	
	464(<0.1)[45]	B_3	
	463(24)[0]	A	
397(13)	407(<0.1)[183]	B_3	ν(Hg-O)
	392(17)[<0.1]	B_2	

exptl $[Hg_2(OTeF_5)_6]^{2-}$ in $[N(CH_3)_4]_2[Hg_2(OTeF_5)_6]$[a,b]	calcd $[Hg_2(OTeF_5)_6]^{2-}$ (D_2)[a,c,d]		
			assgnts
	343(<1)[0]	A	$\delta(TeF_{4e})_{umb}$
341(14)	337(1)[<0.1]	B_3	δ(F-Te-F) / ρ_w(F-Te-F)
	337(<0.1)[53]	B_2	
	334(<0.1)[203]	B_1	δ(F-Te-F) / ρ_w(F-Te-F) / $\delta(TeF_{4e})_{umb}$
334(23)	334(<0.1)[53]	B_3	Te-F stretches
330(22)	334(1)[0]	A	
	334(2)[32]	B_2	
	333(<0.1)[205]	B_3	
	332(<0.1)[28]	B_1	$\delta(TeF_{4e})_{umb}$ / δ(F-Te-F)
327(22)	331(<1)[0]	A	$\delta(TeF_{4e})_{umb}$
	331(<0.1)[41]	B_2	δ(F-Te-O)
	329(<1)[26]	B_3	δ(F-Te-O) / δ(F-Te-F)
	329(11)[111]	B_2	
	329(<1)[17]	B_1	δ(F-Te-F) / ρ_w(F-Te-F)
	329(1)[0]	A	δ(F-Te-F)
322(32)	327(4)[4]	B_3	δ(F-Te-O)
	326(1)[9]	B_1	δ(F-Te-F) / ρ_w(F-Te-F)
	326(<1)[38]	B_2	
	325(<0.1)[27]	B_3	
	324(<0.1)[71]	B_2	δ(F-Te-F)
316(57)	320(<0.1)[80]	B_1	δ(O-Hg-O)$_{o.o.p.}$
	316(3)[<0.1]	B_2	
	312(<1)[0]	A	ρ_t(O-Hg-O)
	309(<1)[3]	B_3	
296(31)	290(3)[0]	A	δ(F-Te-F_e)
	290(2)[<0.1]	B_3	
	289(1)[<1]	B_1	
	289(<1)[<1]	B_2	
	286(2)[<0.1]	B_1	
	286(<0.1)[0]	A	
233(9)	233(<0.1)[<1]	B_2	δ(F-Te-F) / ρ_w(F-Te-F)
	233(1)[<1]	B_1	
	228(<0.1)[12]	B_3	
	228(4)[0]	A	
226(12)	212(<0.1)[<1]	B_1	ρ_w(F-Te-F)
	212(<0.1)[0]	A	
	212(<0.1)[<0.1]	B_3	
	212(<0.1)[<0.1]	B_2	
	212(<0.1)[0]	A	
	211(<0.1)[<1]	B_1	
130(31)	121(<0.1)[2]	B_3	$\rho_t(F_{4e}F_aTe)$
	121(3)[0]	A	

[a]Frequencies are given in cm^{-1}. [b]Values in parentheses denote relative Raman intensities. The Raman spectrum was recorded in an FEP sample tube at −150 °C using 1064-nm excitation. The abbreviations denote shoulder (sh), broad (br), and not observed (n.o.). [c]Values in parentheses denote calculated Raman intensities ($Å^4$ amu^{-1}), whereas values in square brackets denote calculated infrared intensities (km mol^{-1}). Assignments are for the energy-minimized geometry calculated at the PBE1PBE/def2-TZVPP level; only general descriptions of the vibrational modes are listed. The abbreviations denote umbrella (umb), equatorial (4e, where the four F_e atoms are in-phase), axial (a), stretch (ν), bend (δ), twist (ρ_t), wag (ρ_w), and rock (ρ_r). [d]See Table S9 of the Supporting Information for a complete listing of frequencies and detailed descriptions of the assignments.

and 2.230(5) Å; $[N(CH_2CH_3)_4]^+$ salt: 2.262(2) and 2.266(2)/2.259(2) and 2.265(2) Å) and three slightly longer Hg−O bonds ($[N(CH_3)_4]^+$ salt: 2.318(5), 2.323(4) and 2.301(5) Å; $[N(CH_2CH_3)_4]^+$ salt: 2.290(2), 2.297(2) and 2.319(2)/2.276(2), 2.313(2) and 2.317(2) Å). The relative Hg−O_{ax} and Hg−O_{eq} bond lengths of the trigonal bipyramidal $[Hg(OTeF_5)_5]^{3-}$ anion are opposite to those normally encountered for trigonal bipyramidal main-group species, i.e., E−X_{eq} < E−X_{ax}.[45] The difference presumably results from greater steric interactions among the F_5TeO_{eq}-groups in the equatorial plane and with the F_5TeO_{ax}− group. The calculated Te−O_{eq} bonds (1.777−1.779 Å) are shorter than the calculated Te−O_{ax} bonds (1.806−1.808 Å), consistent with Hg−O_{eq} > Hg−O_{ax}. Correspondingly, the Te−F_{ax} and Te−F_{eq} bond lengths of both axial groups are shorter than those of the equatorial groups.

Although the calculated gas-phase geometry of $[Hg(OTeF_5)_5]^{3-}$ differs from that observed in the solid state, the calculated vibrational frequencies and intensities can be used to aid in the assignment of the experimental spectrum. However, it is not possible to discriminate between the vibrational bands arising from the axial or equatorial F_5TeO− groups.

(c) $[Hg_2(OTeF_5)_6]^{2-}$. The calculated structure of the $[Hg_2(OTeF_5)_6]^{2-}$ anion optimized to D_2 symmetry and provided a valid model for the dimeric $[Hg_2(OTeF_5)_6]^{2-}$ anion observed in the crystal structure (Figure 3). The main features observed in the solid-state structure were reproduced, except for the conformations of the $Hg(OTeF_5)_2$ groups, which both optimized to a *syn*-conformation (dihedral Te−O_t−Hg−O_t−Te angle, 12.1°) instead of the observed *anti*- (122.3(3)°) and *gauche*- (34.7(5)°) conformations.[27] Discrepancies between the calculated and observed conformations are likely the result of the secondary interionic Hg---F contacts between dimers in the solid state, which are absent in the model anion.

The Hg and O_μ atoms of the calculated $[HgO_\mu]_2$ core are coplanar by symmetry. The core has geometrical parameters that are in excellent agreement with the experimental values (calcd: ∠O_μ−Hg−O_μ, 72.8°, ∠Hg−O_μ−Hg, 107.2°, Hg−O_μ, 2.441 Å; exptl: ∠O_μ−Hg−O_μ, 70.1(1) and 73.9(1)°, ∠Hg−O_μ−Hg, 102.1(1) and 104.6(1)°, Hg−O_μ, 2.353(4)−2.507(4) Å). The Hg−O_t bond lengths (2.081 Å) are significantly shorter than the Hg−O_μ bond lengths but are only slightly elongated with respect to those of neutral $Hg(OTeF_5)_2$ (2.008 Å).[27] Both Hg−O_μ bonds are elongated compared to the calculated Hg−O bond lengths of $[Hg(OTeF_5)_4]^{2-}$ (2.226 Å) but are slightly shorter than the three equatorial Hg−O bonds (2.481−2.510 Å) in the optimized gas-phase geometry of $[Hg(OTeF_5)_5]^{3-}$ (vide supra).

DOI: 10.1021/ic502602p
Inorg. Chem. 2015, 54, 1606−1626

Table 10. Experimental Raman Frequencies and Intensities for $Cs_2[Hg(OTeF_5)_4]\cdot Hg(OTeF_5)_2$ and Calculated Vibrational Frequencies and Intensities for $[Hg_3(OTeF_5)_8]^{2-}$

exptl [a,b] $Cs_2[Hg(OTeF_5)_4]\cdot Hg(OTeF_5)_2$	calcd [a,c,d] $[Hg_3(OTeF_5)_8]^{2-}$ (C_1)	assgnts
866(40)	853(120)[8]	$[\nu(Hg\text{-}O) - \nu(Te\text{-}O)]_t$ + $[\nu(Hg\text{-}O) - \nu(Te\text{-}O)]_c$
826(10), br	834(8)[382] 826(14)[398] 823(20)[310]	$[\nu(Hg\text{-}O) - \nu(Te\text{-}O)]_t$ / $[\nu(Hg\text{-}O) - \nu(Te\text{-}O)]_c$
816(3)	814(5)[69] 812(18)[205]	
795(sh) 790(6) 780(2) 776(2)	792(1)[583] 791(1)[558]	$[\nu(Hg\text{-}O) - \nu(Te\text{-}O)]_c$
721(15)	707(13)[37] 706(3)[202] 702(2)[10] 697(<1)[82]	$[\nu(Te\text{-}F)]_t$
715(19) 713(19) 710(23) 696(100)	708(7)[107] 706(4)[155] 705(1)[363] 705(6)[151] 704(1)[424] 681(167)[<1]	$[\nu(Te\text{-}F)]_t$ / $[\nu(Te\text{-}F)]_c$
691(sh)	699(<1)[29] 699(1)[21] 696(<1)[387] 695(1)[45]	
688(sh)	692(9)[3] 689(1)[4] 688(1)[5]	$[\nu(Te\text{-}F)]_c$
676(21) 671(sh)	678(3)[245] 678(8)[9] 677(5)[61] 677(2)[73] 677(2)[121] 676(7)[80]	$[\nu(Te\text{-}F)]_t$ / $[\nu(Te\text{-}F)]_c$
653(6)	674(10)[102]	
644(6)	631(<0.1)[1] 630(1)[2] 629(2)[1] 629(3)[<1]	$[\nu(Te\text{-}F)]_t$
628(35)	633(34)[<0.1]	
621(19)	628(4)[<1] 627(6)[<1]	
613(16)	627(<1)[<1] 626(8)[2] 624(3)[4]	$[\nu(Te\text{-}F)]_t$ / $[\nu(Te\text{-}F)]_c$
610(19) 604(sh)	623(8)[<1]	
n.o.	624(1)[1] 623(<1)[1]	$[\nu(Te\text{-}F)]_t$
n.o.	627(<1)[<1] 620(<1)[<1] 620(<1)[<1]	$[\nu(Te\text{-}F)]_c$
492(sh)	499(<1)[40] 498(<1)[40]	$[\nu(Hg\text{-}O) + \nu(Te\text{-}O)]_t$
488(6) 483(6)	488(18)[24] 487(14)[32]	
448(8)	444(24)[<1] 435(<1)[393]	$[\nu(Hg\text{-}O)]_c$ / $[\nu(Hg\text{-}O)]_t$
430(15)	419(9)[3] 419(9)[<1]	
353(10)	345(1)[<1]	$[\delta(TeF_{4e})_{umb}]_t$ / $[\delta(TeF_{4e})_{umb}]_c$
349(10)	338(<1)[2] 336(<0.1)[155] 336(<1)[127]	$[\delta(TeF_{4e})_{umb}]_c$
	336(<1)[159]	$[\delta(F\text{-}Te\text{-}F)]_c$
334(8)	334(<1)[156] 334(<0.1)[154]	$[\delta(TeF_{4e})_{umb}]_c$ / $[\delta(F\text{-}Te\text{-}F)]_t$
	334(<0.1)[41] 334(<1)[27]	$[\delta(F\text{-}Te\text{-}F)]_t$ / $[\delta(F\text{-}Te\text{-}F)]_c$ / $[\rho_w(F\text{-}Te\text{-}F)]_c$
330(10)	333(<1)[24] 333(<1)[8]	$[\delta(TeF_{4e})_{umb}]_t$
327(11)	332(1)[5]	$[\delta(F\text{-}Te\text{-}F)]_t$ / $[\delta(F\text{-}Te\text{-}F)]_c$
321(6)	332(<1)[1] 332(<1)[13] 331(<1)[24] 330(<1)[25]	$[\delta(F\text{-}Te\text{-}F)]_t$ / $[\delta(F\text{-}Te\text{-}O)]_t$
317(5)	329(1)[12] 328(2)[21] 328(3)[65] 327(1)[63] 327(3)[42] 326(<1)[32] 325(<1)[18] 323(<1)[11]	$[\delta(F\text{-}Te\text{-}F)]_t$ / $[\delta(F\text{-}Te\text{-}O)]_t$ / $[\delta(F\text{-}Te\text{-}F)]_c$ / $[\delta(F\text{-}Te\text{-}O)]_c$
	323(<1)[10]	$[\delta(F\text{-}Te\text{-}F)]_c$ / $[\rho_w(O\text{-}Hg\text{-}O)]_t$
n.o.	322(<0.1)[12] 321(<0.1)[76]	$[\delta(O\text{-}Te\text{-}F)]_t$ / $[\rho_t(O\text{-}Hg\text{-}O)]_c$ $[\delta(F\text{-}Te\text{-}F)]_c$
	319(2)[3] 319(2)[4]	$[\delta(F\text{-}Te\text{-}F)_c$ / $[\rho_w(O\text{-}Hg\text{-}O)]t$
305(sh)	313(<1)[6] 312(<0.1)[2] 293(1)[<1] 293(1)[<1] 292(1)[<1] 291(1)[<1]	$[\delta(F\text{-}Te\text{-}F)]_t$
298(19)	321(<0.1)[9] 290(<1)[<1] 290(2)[<0.1] 290(2)[<0.1] 289(<0.1)[<0.1]	$[\delta(F\text{-}Te\text{-}F)]_c$
235(6)	242(<1)[<0.1] 241(<1)[<1] 233(2)[6] 231(2)[6]	$[\delta(F\text{-}Te\text{-}F)]_t$ / $[\rho_w(F\text{-}Te\text{-}F)]_t$
	216(2)[<0.1] 214(<0.1)[1]	$[\delta(F\text{-}Te\text{-}F)]_c$
204(2)	213(<0.1)[<0.1] 212(<0.1)[<1] 212(<0.1)[<1] 212(<0.1)[<1] 212(<0.1)[<1] 212(<0.1)[<1] 211(<1)[<0.1] 211(<0.1)[<0.1]	$[\rho_w(F\text{-}Te\text{-}F)]_t$ / $[\rho_w(F\text{-}Te\text{-}F)]_c$
n.o.	209(<0.1)[1] 209(<0.1)[1] 202(<0.1)[<1] 202(<0.1)[<1] 202(<0.1)[<0.1] 201(<0.1)[<0.1]	$[\rho_w(O\text{-}Te\text{-}F)]_t$ / $[\rho_w(O\text{-}Te\text{-}F)]_c$
n.o.	201(<0.1)[<0.1] 200(<1)[<1] 193(<0.1)[<1] 190(<0.1)[<0.1]	$[\rho_w(O\text{-}Te\text{-}F)]_t$ / $[\rho_w(F\text{-}Te\text{-}F)]_t$
150(6)	159(<1)[5] 158(<1)[5]	
n.o.	142(<0.1)[4]	
128(16)	126(2)[<1] 126(<1)[3]	$[\rho_r(F_{2e}F_aTe)]_t$

[a] Frequencies are given in cm^{-1}. [b] Values in parentheses denote relative Raman intensities. The Raman spectrum was recorded in an FEP sample tube at −150 °C using 1064-nm excitation. The abbreviations denote shoulder (sh), broad (br), and not observed (n.o.). [c] Values in parentheses denote calculated Raman intensities ($Å^4$ amu^{-1}), whereas values in square brackets denote calculated infrared intensities (km mol^{-1}). Assignments are for the energy-minimized geometry calculated at the PBE1PBE/def2-TZVPP level; only general descriptions of the vibrational modes are listed. The abbreviations denote umbrella (umb), equatorial (4e, where the four F_e atoms are in-phase), axial (a), stretch (ν), bend (δ), twist (ρ_t), wag (ρ_w), and rock (ρ_r). [d] See Table S10 of the Supporting Information for a complete listing of frequencies and detailed descriptions of the assignments.

The calculated O_t−Hg−O_t bond angles (162.5°) are intermediate with respect to those subtended at $Hg_{(2)}$ (157.0(2)°) and $Hg_{(1)}$ (174.1(2)°) in the crystal structure. The calculated Te−O_μ bond lengths (1.810 Å) are slightly shorter than the Te−O_t bond lengths (1.821 Å), a trend that is also observed in the crystal structure (Te−O_μ, 1.788(4)−1.800(4) Å; Te−O_t, 1.811(4)−1.821(4) Å). There are no significant differences among the calculated Te−F bond lengths and angles of F_5TeO− groups in either the calculated or experimental structures.

DOI: 10.1021/ic502602p
Inorg. Chem. 2015, 54, 1606−1626

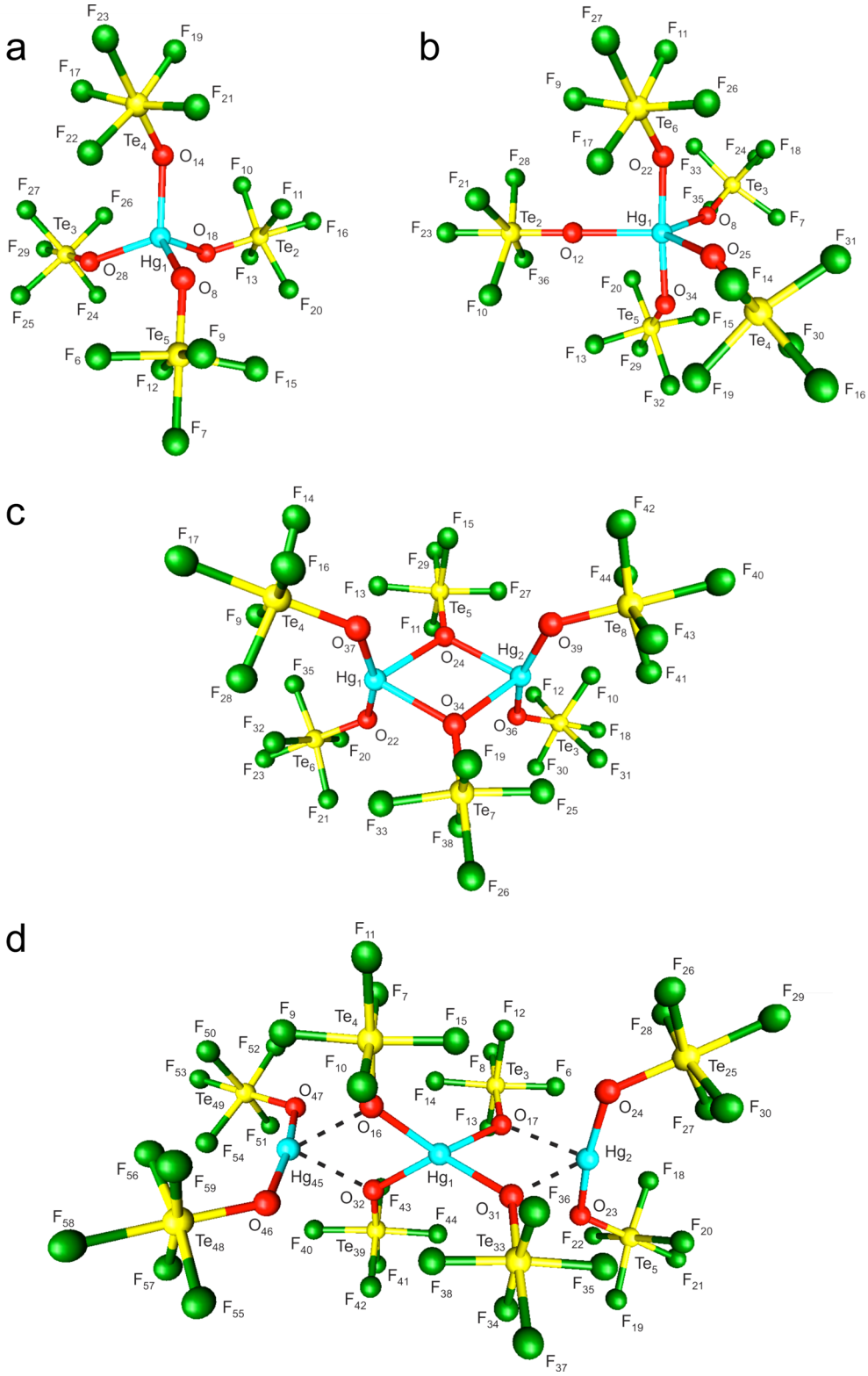

Figure 10. Gas-phase energy-minimized geometries of (a) $[Hg(OTeF_5)_4]^{2-}$ (S_4), (b) $[Hg(OTeF_5)_5]^{3-}$ (C_1), (c) $[Hg_2(OTeF_5)_6]^{2-}$ (D_2), and (d) $[Hg_3(OTeF_5)_8]^{2-}$ (C_1) calculated at the PBE1PBE/def2-TZVPP level of theory. Long contacts between the central "$[Hg(OTeF_5)_4]^{2-}$ unit" and terminal "$Hg(OTeF_5)_2$ units" are indicated by dashed lines.

(d) $[Hg_3(OTeF_5)_8]^{2-}$. The calculated structure of the unknown $[Hg_3(OTeF_5)_8]^{2-}$ anion (Figure 10d) was used to model the Hg environments present in the crystal structure of $Cs_2[Hg(OTeF_5)_4]\cdot Hg(OTeF_5)_2$ and the vibrational modes of this compound (see Raman Spectroscopy).

The environment around the central Hg_2 atom is very well reproduced. The Hg–O bond lengths (2.231–2.241 Å) of the central $[Hg(OTeF_5)_4]^{2-}$ unit are intermediate with respect to the experimental Hg_2–O values (2 × 2.186(1) Å and 2 × 2.287(1) Å). The environment around the central Hg atom is a distorted

DOI: 10.1021/ic502602p
Inorg. Chem. 2015, 54, 1606–1626

tetrahedron with O−Hg−O bond angles that are significantly larger (calcd, 126.6 and 128.7°; exptl, 137.9(1) and 147.8(1)°) and smaller (calcd, 77.8 and 77.8°; exptl, 110.4(1) and 81.4(1)°) than the ideal tetrahedral angle, 109.5°. As observed in the crystal structure, the four oxygen atoms of the central $[Hg(OTeF_5)_4]^{2-}$ unit interact with two $Hg(OTeF_5)_2$ units through Hg---O contacts (calcd, 2.554−2.564 Å), in good agreement with the experimental values (2 × 2.555(1) and 2 × 2.737(1) Å). The Hg---F contacts to fluorine atoms of adjacent $Hg(OTeF_5)_2$ units are absent in the gas-phase structure because both terminal $Hg(OTeF_5)_2$ units adopt *syn*-conformations.

The calculated Te−O (1.823−1.824 Å) bond lengths of the central $[Hg(OTeF_5)_4]^{2-}$ unit are slightly elongated when compared to its experimental values (1.798(1) and 1.816(1) Å), and those of the isolated $[Hg(OTeF_5)_4]^{2-}$ anion (calcd, 1.799 Å; exptl, 1.797(6) Å). The Te−F bond lengths (1.852−1.866 Å) are in good agreement with the experimental values (1.838(1)−1.865(1) Å) with no significant differences between the axial and equatorial bond lengths.

Both terminal $Hg(OTeF_5)_2$ units of the calculated $[Hg_3(OTeF_5)_8]^{2-}$ anion adopt *syn*-conformations (dihedral $Te_5-O_{23}-Hg_2-O_{24}-Te_{25}$ angle, 15.0°; dihedral $Te_{49}-O_{47}-Hg_{45}-O_{46}-Te_{48}$ angle, 2.2°), in contrast with the *anti*-conformation (dihedral Te−O−Hg−O−Te angle, 139.1°) that is present in the solid state (Figure 4). Despite this conformational difference and because the model takes into account some of the interactions with the $[Hg(OTeF_5)_4]^{2-}$ unit, the overall trends in geometrical parameters and vibrational frequencies are very well reproduced.

The calculated Hg−O bond lengths (2.039−2.041 Å) are elongated compared to monomeric $Hg(OTeF_5)_2$ (1.976 Å).[27] As observed experimentally, the elongations of the Hg−O bonds are attributable to additional Hg---O contacts. Correspondingly, the calculated Te−O bond lengths (1.829−1.830 Å) are shorter than in $Hg(OTeF_5)_2$ (1.856 Å). The calculated Te−F bond lengths (1.847−1.864 Å) do not differ significantly from those of $Hg(OTeF_5)_2$ (1.835−1.866 Å). The calculated O−Hg−O bond angles (172.0 and 172.2°) are very close to the corresponding bond angle in $Hg(OTeF_5)_2$ (177.0°).

Natural Bond Orbital (NBO) Analyses, Charges, Valencies, and Bond Orders. *(a) $[Hg(OTeF_5)_4]^{2-}$ and $[Hg(OTeF_5)_5]^{3-}$.* The Hg charges are significantly more positive in the anions (1.689 and 1.675, respectively) than in neutral $Hg(OTeF_5)_2$ (1.422) (Tables S17 and S18, Supporting Information). The highest negative charges reside on the O atoms and are somewhat more negative for the 2− anion (4 × −1.235) than for the 3− anion (ax: 2 × −1.202; eq: −1.202, −1.203, −1.210). The Hg−O bond orders are significantly less in $[Hg(OTeF_5)_4]^{2-}$ (4 × 0.115) and $[Hg(OTeF_5)_5]^{3-}$ (ax: 2 × 0.170; eq: 2 × 0.036 and 0.034) than in $Hg(OTeF_5)_2$ (0.291), consistent with more polar Hg−O bonds in the anions than in neutral $Hg(OTeF_5)_2$. Correspondingly, the Te−O bond orders are greater in $[Hg(OTeF_5)_4]^{2-}$ (4 × 0.784) and $[Hg(OTeF_5)_5]^{3-}$ (ax: 2 × 0.766; eq: 2 × 0.841 and 0.846) anions than in $Hg(OTeF_5)_2$ (0.672). Overall, the teflate groups of the anions accommodate significantly more negative charge than those of $Hg(OTeF_5)_2$, as reflected by the average total F_5TeO- group charges ($Hg(OTeF_5)_2$, −0.711; $[Hg(OTeF_5)_4]^{2-}$, −0.922; $[Hg(OTeF_5)_5]^{3-}$, −0.934). Most of the negative charge of the $[Hg(OTeF_5)_5]^{3-}$ anion is located on the $F_5TeO_{eq}-$ groups ($F_5TeO_{eq}-$, −0.981; $F_5TeO_{ax}-$, −0.863). The charge difference is consistent with the calculated Te−O_{eq} bond lengths where $Te-O_{eq} > Te-O_{ax}$ (Table S13, Supporting Information). The Hg valencies of $[Hg(OTeF_5)_4]^{2-}$ (0.455) and $[Hg(OTeF_5)_5]^{3-}$ (0.444) when compared to that of $Hg(OTeF_5)_2$ (0.602) are also consistent with the enhanced polarities of the Hg−O bonds in the anions.

(b) $[Hg_2(OTeF_5)_6]^{2-}$. The charges on the terminal Hg_1 and Hg_2 atoms (1.470) (Table S19, Supporting Information, Figure 10c) are little affected by contacts with $[OTeF_5]^-$ when compared with gas-phase $Hg(OTeF_5)_2$ (1.422). The highest negative charges reside on the O atoms, with charges on the terminal O_t atoms (−1.197) that are slightly more negative than in $Hg(OTeF_5)_2$ (−1.176). This is accompanied by a decrease in the Hg−O_t bond orders (0.183) with respect to those of $Hg(OTeF_5)_2$ (0.291) and an increase in the Te−O_t bond orders (0.741) with respect to those of $Hg(OTeF_5)_2$ (0.672). The charges on the bridging O_μ atoms (−1.297) are more negative than those of O_t (−1.197) and the $[OTeF_5]^-$ anion (−1.127). The Te−O_μ bond orders (0.754) are less than that of the $[OTeF_5]^-$ anion (0.866), consistent with bridge formation and decreased π character of the Te−O_μ bond. The small Hg_1-O_μ bridge bond orders (0.020) are consistent with rather weak covalent interactions between the $Hg(OTeF_5)_2$ acceptor and the $F_5TeO_\mu-$ ligand.

CONCLUSION

The coordination behavior of $Hg(OTeF_5)_2$ toward the $[OTeF_5]^-$ anion was investigated by reactions of $Hg(OTeF_5)_2$ with $[M][OTeF_5]$ ($M^+ = [N(CH_3)_4]^+$, $[N(CH_2CH_3)_4]^+$, Cs^+). The resulting salts, $[N(CH_2CH_3)_4]_2[Hg(OTeF_5)_4]$, $[N(CH_3)_4]_3[Hg(OTeF_5)_5]$, $[N(CH_2CH_3)_4]_3[Hg(OTeF_5)_5]$, $[N(CH_3)_4]_2[Hg_2(OTeF_5)_6]$, $Cs_2[Hg(OTeF_5)_4]\cdot Hg(OTeF_5)_2$, and $\{Cs_3[Hg_2(OTeF_5)_7]\cdot Hg(OTeF_5)_2\}\cdot 4SO_2ClF$, were characterized in the solid state by single-crystal X-ray diffraction. The $[Hg(OTeF_5)_4]^{2-}$ anion of the $[N(CH_2CH_3)_4]^+$ salt is well isolated, having nearly ideal tetrahedral coordination at Hg(II). In contrast, the $[Hg(OTeF_5)_4]^{2-}$ anion of $Cs_2[Hg(OTeF_5)_4]\cdot Hg(OTeF_5)_2$ comprises part of a chain structure in which it weakly interacts with $Hg(OTeF_5)_2$, resulting in a flattened $[Hg(OTeF_5)_4]^{2-}$ tetrahedron. The $[N(CH_3)_4]_3[Hg(OTeF_5)_5]$ and $[N(CH_2CH_3)_4]_3[Hg(OTeF_5)_5]$ salts contain well-isolated $[Hg(OTeF_5)_5]^{3-}$ anions having distorted square-pyramidal geometries that contrast with the energy-minimized trigonal bipyramidal geometry calculated for the gas-phase anion. The occurrence of significant cation−anion contacts and an intraionic Hg---F interaction likely accounts for the square-pyramidal geometry in the solid state. Although attempts to form the $[Hg(OTeF_5)_3]^-$ anion failed, its dimer, $[Hg_2(OTeF_5)_6]^{2-}$, has been isolated as the $[N(CH_3)_4]^+$ salt in which two $Hg(OTeF_5)_2$ moieties are linked to each other through two bridging F_5TeO- groups. The structure of the $[Hg_2(OTeF_5)_7]^{3-}$ anion may be formulated as two $[Hg(OTeF_5)_3]^-$ anions bridged by a $[OTeF_5]^-$ anion. This anion also participates in a chain structure in which it alternates and interacts with $Hg(OTeF_5)_2$ molecules. Attempts to synthesize salts of the $[Hg(OTeF_5)_6]^{4-}$ anion only yielded $[Hg(OTeF_5)_4]^{2-}$ and $[Hg(OTeF_5)_5]^{3-}$.

Quantum-chemical calculations have been used to model the gas-phase geometries of the $[Hg(OTeF_5)_4]^{2-}$, $[Hg(OTeF_5)_5]^{3-}$ and $[Hg_2(OTeF_5)_6]^{2-}$ anions and the hypothetical $[Hg_3(OTeF_5)_8]^{2-}$ anion. Their calculated vibrational frequencies and intensities aided in the assignment of the Raman spectra of $[N(CH_2CH_3)_4]_2[Hg(OTeF_5)_4]$, $[N(CH_3)_4]_3[Hg(OTeF_5)_5]$, $[N(CH_2CH_3)_4]_3[Hg(OTeF_5)_5]$, and $Cs_2[Hg(OTeF_5)_4]\cdot Hg(OTeF_5)_2$. The NBO analyses show that the Hg−O bonds of the gas-phase $[Hg(OTeF_5)_4]^{2-}$ and $[Hg(OTeF_5)_5]^{3-}$ anions

DOI: 10.1021/ic502602p
Inorg. Chem. 2015, 54, 1606−1626

are similar and significantly more polar than the Hg−O bonds in $Hg(OTeF_5)_2$.

The $[Hg(OTeF_5)_4]^{2-}$, $[Hg_2(OTeF_5)_6]^{2-}$, and $[Hg_2(OTeF_5)_7]^{3-}$ anions exhibit structural features that are in common with their chlorine, bromine, and iodine analogues and provide rare examples of teflate derivatives that contain bridging F_5TeO- groups. The square-pyramidal $[Hg(OTeF_5)_5]^{3-}$ anion is the first teflate anion to be isolated that bares a 3− charge. Its geometry contrasts with the trigonal bipyramidal geometries of the $[HgX_5]^{3-}$ (X = Cl, Br) anions in the solid state and with the calculated trigonal bipyramidal gas-phase geometry of $[Hg(OTeF_5)_5]^{3-}$.

EXPERIMENTAL SECTION

Apparatus and Materials. *(a) General.* Manipulations involving air-sensitive materials were carried out under anhydrous conditions on glass and metal high-vacuum lines and inside an inert atmosphere drybox as previously described.[51] Preparative work was carried out in T-shaped reaction vessels constructed from $^1/_4$-in. o.d. ($^1/_{16}$-in. wall thickness) lengths of FEP (tetrafluoroethylene-hexafluoropropylene block copolymer) tubing. The tubing was heat-sealed at one end, heat flared at the other end, and connected through a 45° SAE flare nut to the conical end of a Kel-F (chlorotrifluoroethylene polymer) valve to form a compression seal. Reaction vessels and sample tubes were rigorously dried under dynamic vacuum prior to passivation for at least 8 h with 1 atm of F_2 gas. Vacuum line connections were made using $^1/_4$-in. 316 stainless steel Swagelok Ultratorr unions fitted with Viton O-rings.

Literature methods were used to prepare $Hg(OTeF_5)_2$,[27] $Cs[OTeF_5]$,[52] $[N(CH_3)_4][OTeF_5]$,[53] and $[N(CH_2CH_3)_4][OTeF_5]$[54] in high purity and to purify SO_2ClF (Allied Chemical, Baker Adamson Division).[55] Methylene chloride (Caledon, reagent grade) was dried over previously vacuum-dried (250 °C) Davison type 3 Å molecular sieves (Fisher Scientific) for 3 days followed by vacuum distillation into a dry glass bulb equipped with a 4-mm J. Young (glass/Teflon) valve. Industrial grade N_2 (99.995%, Praxair) gas was used for backfilling reaction and sample vessels. Sulfur dioxide (Aldrich) was dried over P_4O_{10} followed by vacuum distillation.

(b) Syntheses and Crystal Growth. Reagents were combined in $^1/_4$-in. o.d. T-shaped FEP reaction vessels at room temperature inside of a drybox. The vessels were then transferred onto a glass vacuum line where the solvent was vacuum distilled and condensed onto the reactants. All crystal growing was carried out under a reduced N_2 pressure by slow evaporation of the solvent at 0 °C into the side arm of the reaction vessel, which was cooled to −78 °C using a dry ice/acetone bath. The side arm containing the condensed solvent was then cooled to −196 °C and heat-sealed off under dynamic vacuum. Unless otherwise stated, the low-temperature Raman spectra (−150 °C) were recorded directly on the freshly crystallized sample.

(i) $[N(CH_2CH_3)_4]_2[Hg(OTeF_5)_4]$. The reaction vessel was loaded with $Hg(OTeF_5)_2$ (0.0476 g, 0.0702 mmol) and $[N(CH_2CH_3)_4][OTeF_5]$ (0.0510, 0.1382 mmol) followed by condensation of ∼0.4 mL of SO_2ClF solvent onto the reagents at −78 °C. The void above the solution was backfilled with 300 Torr of dry N_2 and warmed to room temperature for 1 h to solubilize and allow the reagents to fully react. Slow evaporation of the solvent into the side arm of the reaction vessel was complete after 16 h, leaving behind a deposit of colorless, plate-shaped crystals on the walls of the FEP reactor. A $[N(CH_2CH_3)_4]_2[Hg(OTeF_5)_4]$ crystal having the dimensions 0.06 mm × 0.10 mm × 0.14 mm was selected for a low-temperature X-ray structure determination.

(ii) $[N(CH_3)_4]_3[Hg(OTeF_5)_5]$. The reagents, $Hg(OTeF_5)_2$ (0.0937 g, 0.1383 mmol) and $[N(CH_3)_4][OTeF_5]$ (0.0970, 0.3103 mmol), were combined in an FEP reaction vessel and SO_2 (∼0.3 mL) was condensed onto the reagents at −78 °C. The reactor and contents were backfilled to 760 Torr with dry N_2. When warmed to 0 °C, the reagents completely dissolved. Crystals were grown by evaporation over a 7 h period and resulted in colorless plate-shaped crystals. A $[N(CH_3)_4]_3[Hg(OTeF_5)_5]$ crystal having the dimensions 0.10 mm × 0.15 mm × 0.26 mm was selected for a low-temperature X-ray structure determination.

(iii) $[N(CH_2CH_3)_4]_3[Hg(OTeF_5)_5]$. The starting materials, $Hg(OTeF_5)_2$ (0.0274 g, 0.0404 mmol) and $[N(CH_2CH_3)_4][OTeF_5]$ (0.0574 g, 0.1556 mmol), were combined inside an FEP reaction vessel, and SO_2ClF (∼0.5 mL) was condensed onto the reagents at −78 °C. The reaction vessel and contents were backfilled with 300 Torr of dry N_2. The reaction mixture was allowed to stand at room temperature for 3 h to solubilize and react. Crystal growth by slow evaporation was complete after 17 h, leaving behind a deposit of colorless plate-shaped crystals on the walls of the FEP reactor. The Raman spectrum was not obtained for this salt. A crystal of $[N(CH_2CH_3)_4]_3[Hg(OTeF_5)_5]$ having the dimensions 0.08 mm × 0.08mm × 0.15 mm was selected for a low-temperature X-ray structure determination.

(iv) $[N(CH_3)_4]_2[Hg_2(OTeF_5)_6]$. In a typical synthesis, $Hg(OTeF_5)_2$ (0.0485, 0.0715 mmol) and $[N(CH_3)_4][OTeF_5]$ (0.0204, 0.0651 mmol) were weighed out and added to an FEP reaction vessel. Approximately 0.25 mL of CH_2Cl_2 was condensed onto the reagents and the reactor and contents were backfilled to 100 Torr with dry N_2. The reaction vessel was warmed to room temperature for 5 h to allow complete dissolution and reaction. Crystal growth was induced by slow evaporation of the solvent over 16 h which resulted in the formation of colorless, tetragonal prisms. A $[N(CH_3)_4]_2[Hg_2(OTeF_5)_6]$ crystal having the dimensions 0.05 mm × 0.05 mm × 0.16 mm was selected for a low-temperature X-ray structure determination.

(v) $Cs_2[Hg(OTeF_5)_4]\cdot Hg(OTeF_5)_2$ and $\{Cs_3[Hg_2(OTeF_5)_7]\cdot Hg(OTeF_5)_2\}\cdot 4SO_2ClF$. In the ensuing description, parentheses denote quantities used for the synthesis of $Cs_2[Hg(OTeF_5)_4]\cdot Hg(OTeF_5)_2$ and square brackets denote quantities used for the synthesis of $\{Cs_3[Hg_2(OTeF_5)_7]\cdot Hg(OTeF_5)_2\}\cdot 4SO_2ClF$. Although a wide range of molar ratios were investigated, no other salts were isolated.

In a typical synthesis, the reaction vessel was loaded with $Hg(OTeF_5)_2$ (0.0639 g, 0.0439 mmol) [0.0765 g, 0.1129 mmol] and $Cs[OTeF_5]$ (0.0297 g, 0.1719 mmol) [0.0858 g, 0.2308 mmol] followed by condensation of ∼0.3 mL of SO_2ClF solvent onto the reagents at −78 °C. The voids above the solutions were backfilled with 400 Torr of dry N_2 and the reaction mixtures were warmed to room temperature for 3 h. Solvent evaporation was complete after 16 h, and resulted in the formation of colorless, plate-shaped crystals. The Raman spectrum was not obtained for the SO_2ClF solvate. Crystals having the dimensions 0.06 mm × 0.15 mm × 0.18 mm [0.11 mm × 0.11 mm × 0.40 mm] were selected for a low-temperature X-ray structure determination.

(vi) Attempted Syntheses of $[N(CH_2CH_3)_4][Hg(OTeF_5)_3]$ and $[N(CH_2CH_3)_4]_4[Hg(OTeF_5)_6]$. Several reactions between $Hg(OTeF_5)_2$ and $[N(CH_2CH_3)_4][OTeF_5]$ were attempted with the view to isolate and characterize the $[Hg(OTeF_5)_3]^-$ and $[Hg(OTeF_5)_6]^{4-}$ anions. A range of molar ratios spanning 1:1 to 1:5 for $Hg(OTeF_5)_2$:$[N(CH_2CH_3)_4][OTeF_5]$ were used at scales similar to those described above. A variety of solvents (SO_2ClF, SO_2, and CH_2Cl_2) were used for crystal growth. Reactions using high molar ratios of $[N(CH_2CH_3)_4][OTeF_5]$ only resulted in $[N(CH_2CH_3)_4]_2[Hg(OTeF_5)_4]$ and $[N(CH_2CH_3)_4]_3[Hg(OTeF_5)_5]$ (see above). At low molar ratios, a colorless and vitreous material formed that failed to crystallize. Raman spectra showed bands similar to those of $[N(CH_3)_4]_2[Hg_2(OTeF_5)_6]$, suggesting that $[N(CH_2CH_3)_4]_2[Hg_2(OTeF_5)_6]$ may have formed.

X-ray Crystallography. *(a) Crystal Mounting Procedure.* All crystalline products were stored at −78 °C until a suitable crystal could be selected and mounted on an X-ray diffractometer using a previously described low-temperature crystal mounting technique.[56] Dried crystalline samples that had been maintained at −78 °C were quickly dumped at −78 °C into an aluminum trough that had been cooled to −110 ± 5 °C by means of a cold stream of dry N_2 gas, allowing selection of individual crystals under a stereomicroscope. Crystals were mounted at the tip of a glass fiber at −110 ± 5 °C using a Fomblin oil as the adhesive and transferred onto a goniometer head using cryotongs (Hampton Research) which had been cooled to −196 °C in liquid N_2.[56]

(b) Collection and Reduction of X-ray Data. Crystals were centered on a SMART APEX II diffractometer, equipped with an APEX II 4K charge-coupled device (CCD) and a triple-axis goniometer, controlled by the APEX2 Graphical User Interface (GUI) software.[57] A Bruker Triumph curved crystal monochromator with Mo Kα (λ = 0.71073 Å) was used as the radiation source. For all data sets, the ϕ-rotations were

DOI: 10.1021/ic502602p
Inorg. Chem. 2015, 54, 1606−1626

fixed at $\chi = 54.74°$ and collected at 0.5° intervals, while some required a series of short ω-scans at various ϕ-settings to fill the gaps.

The diffraction data sets of $[N(CH_2CH_3)_4]_2[Hg(OTeF_5)_4]$ and $[N(CH_2CH_3)_4]_3[Hg(OTeF_5)_5]$ (in square brackets) consisted of a half-sphere of ϕ-rotations (1212 [2428] frames) with exposure times of 50 [20] s. The diffraction data collection for $[N(CH_3)_4]_2[Hg_2(OTeF_5)_6]$ consisted of a half-sphere of ϕ-rotations (4979 frames) and a series of ω-scans (613 frames) with exposure times of 2 s. In the case of $[N(CH_3)_4]_3[Hg(OTeF_5)_5]$, a half-sphere of ϕ-rotations (3752 frames) and a series of ω-scans (410 frames) were collected with exposure times of 10 s. The diffraction data sets consisted of a full ϕ-rotation (2686 frames) with exposure times of 3 s for $Cs_2[Hg(OTeF_5)_4]\cdot Hg(OTeF_5)_2$. The diffraction data set for $\{Cs_3[Hg_2(OTeF_5)_7]\cdot Hg(OTeF_5)_2\}\cdot 4SO_2ClF$ consisted of a half-sphere of ω-scans (1212 frames) with 50 s exposure times. The crystal-to-detector distances were 4.9540 cm and the data collection was carried out in a 512 × 512 pixel mode using 2 × 2 pixel binning. All diffraction data were processed by use of the APEX2 GUI software,[57] which applied Lorentz and polarization corrections to three-dimensionally integrated diffraction spots. The program SADABS[58] was used for scaling the diffraction data, the application of a decay correction, and an empirical absorption correction based on redundant reflections.

(c) Solution and Refinement of the Structures. The XPREP[59] program was used to confirm the unit cell dimensions, crystal system, and space group. The structures were solved in their respective space groups by use of direct methods using SHELXS[59] or SIR92,[60] and the solutions yielded the positions of all heavy atoms as well as some of the lighter atoms. Successive difference Fourier syntheses revealed the positions of the remaining light atoms. The final refinements were obtained by introducing anisotropic parameters for all the atoms, an extinction parameter, and the recommended weighting factor. The positions of the hydrogen atoms in the $[N(CH_3)_4]^+$ and $[N(CH_2CH_3)_4]^+$ cations were calculated. The maximum electron densities in the final difference Fourier maps were located around the heavy atoms. The PLATON program[60] could not suggest additional or alternative symmetries.

Refinement of the structure of $Cs_2[Hg(OTeF_5)_4]\cdot Hg(OTeF_5)_2$ was straightforward. In the structure of $\{Cs_3[Hg_2(OTeF_5)_7]\cdot Hg(OTeF_5)_2\}\cdot 4SO_2ClF$, one SO_2ClF molecule ($S_{(3)}$) was found to be disordered between two orientations (72/28) sharing a common central sulfur atom. In the structure of $[N(CH_3)_4]_2[Hg_2(OTeF_5)_6]$, one of the two $[N(CH_3)_4]^+$ cations ($N_{(2)}$) as well as one of the terminal teflate groups ($Te_{(6)}$) were found to be disordered between two orientations (50/50), sharing a common central nitrogen or tellurium atom. For both disordered structures, the disorder was dealt with by using the command SAME.[59] As a consequence, the light atoms of the disordered entities were refined isotropically. The structure of $[N(CH_2CH_3)_4]_2[Hg(OTeF_5)_4]$ was solved in the *Pc* space group and was refined as a racemic twin. For $[N(CH_3)_4]_3[Hg(OTeF_5)_5]$, a satisfactory model was obtained in the *Cc* space group; however, the refinement as a single crystal remained at an overall agreement factor of ca. 0.33, with unsatisfactory behavior for several parameters. With the introduction of the twin matrix ($\bar{1}\,0\,0\,0\,\bar{1}\,0\,0\,0\,1$) characteristic of a pseudomerohedral twin, the refinement converged. A refinement was carried out using this law, giving rise to a drastic drop in R_1 to 0.15, indicating the correct law had been applied. At this stage, the possibilities of a racemic twin or wrong absolute structure were suggested by the program. Although the absolute structure was checked, it was shown that the contribution of a racemic twin had to be taken into consideration. The final twin law used was ($\bar{1}\,0\,0\,0\,\bar{1}\,0\,0\,0\,1\,\bar{4}$), which resulted in a R_1-value of 0.0196. Attempts were made to solve the structure in the *C*2/c space group but were unsuccessful. The structure of $[N(CH_2CH_3)_4]_3[Hg(OTeF_5)_5]$ was solved in the $P2_1$ space group as a racemic twin. Attempts were made to solve this structure in the $P2_1/m$ space group, but were unsuccessful.

Raman Spectroscopy. Raman spectra were recorded on a Bruker RFS 100 FT-Raman spectrometer at −150 to −155 °C using 1064-nm excitation at a laser power of 500 mW, and 1 cm^{-1} resolution as previously described.[56] A total of 1200 scans were acquired for each spectrum. Spectra of the crystalline solids were recorded in $^1/_4$-in. o.d. FEP reaction vessels.

Computational Details. The optimized gas-phase geometries and vibrational frequencies of $[Hg(OTeF_5)_4]^{2-}$, $[Hg(OTeF_5)_5]^{3-}$, $[Hg_2(OTeF_5)_6]^{2-}$, and $[Hg_3(OTeF_5)_8]^{2-}$ were obtained at the PBE1PBE level of theory using the def2-TZVPP basis sets.[61−63] All basis sets were obtained online from the EMSL Basis Set Exchange (https://bse.pnl.gov/bse/portal).[64] The PBE1PBE/def2-TZVPP method was chosen because it has proven reliable for $Hg(OTeF_5)_2$ and $Hg(OTeF_5)_2\cdot 1.5NgF_2$ (Ng = Kr, Xe).[27] Quantum-chemical calculations were carried out using the program Gaussian 09[65] for geometry optimizations, vibrational frequencies, and vibrational band intensities. All geometries were fully optimized using analytical gradient methods. The program, GaussView,[66] was used to visualize the vibrational displacements that form the basis for the vibrational mode descriptions given in Tables 7−10 and Tables S7−S10 of the Supporting Information. Natural bond orbital analyses were performed using the PBE1PBE densities with the NBO program (version 6.0).[50]

■ ASSOCIATED CONTENT

Supporting Information

Complete list of experimental geometrical parameters for $[N(CH_2CH_3)_4]_2[Hg(OTeF_5)_4]$ (Table S1), $[N(CH_3)_4]_3[Hg(OTeF_5)_5]$ (Table S2), $[N(CH_3)_4]_2[Hg_2(OTeF_5)_6]$ (Table S3), $Cs_2[Hg(OTeF_5)_4]\cdot Hg(OTeF_5)_2$ (Table S4), $\{Cs_3[Hg_2(OTeF_5)_7]\cdot Hg(OTeF_5)_2\}\cdot 4SO_2ClF$ (Table S5), and $[N(CH_2CH_3)_4]_3[Hg(OTeF_5)_5]$ (Table S6); asymmetric units of $[N(CH_2CH_3)_4]_2[Hg(OTeF_5)_4]$ (Figure S1), $[N(CH_3)_4]_3[Hg(OTeF_5)_5]$ (Figure S2), $[N(CH_2CH_3)_4]_3[Hg(OTeF_5)_5]$ (Figure S3), and $[N(CH_3)_4]_2[Hg_2(OTeF_5)_6]$ (Figure S4), packing of $Cs_2[Hg(OTeF_5)_4]\cdot Hg(OTeF_5)_2$ (Figure S5) and $\{Cs_3[Hg_2(OTeF_5)_7]\cdot Hg(OTeF_5)_2\}\cdot 4SO_2ClF$ (Figure S6); full Raman spectra of $[N(CH_2CH_3)_4]_2[Hg(OTeF_5)_4]$ (Figure S7), $[N(CH_3)_4]_3[Hg(OTeF_5)_5]$ (Figure S8), and $[N(CH_3)_4]_2[Hg_2(OTeF_5)_6]$ (Figure S9); full listings of calculated vibrational frequencies and intensities and their assignments for $[Hg(OTeF_5)_4]^{2-}$ (Table S7), $[Hg(OTeF_5)_5]^{3-}$ (Table S8), $[Hg_2(OTeF_5)_6]^{2-}$ (Table S9), and $[Hg_3(OTeF_5)_8]^{2-}$ (Table S10); experimental and calculated vibrational data for $[OTeF_5]^-$ (Table S11); calculated geometry of $[OTeF_5]^-$ (Figure S10); complete lists of calculated geometrical parameters for $[Hg(OTeF_5)_4]^{2-}$ (Table S12), $[Hg(OTeF_5)_5]^{3-}$ (Table S13), $[Hg_2(OTeF_5)_6]^{2-}$ (Table S14), $[Hg_3(OTeF_5)_8]^{2-}$ (Table S15), and $[OTeF_5]^-$ (Table S16); NBO valencies, bond orders, and NPA charges for $[Hg(OTeF_5)_4]^{2-}$ (Table S17), $[Hg(OTeF_5)_5]^{3-}$ (Table S18), $[Hg_2(OTeF_5)_6]^{2-}$ (Table S19), $Hg(OTeF_5)_2$ (Table S20), and $[OTeF_5]^-$ (Table S21); X-ray crystallographic files in CIF format for the structure determinations of $[N(CH_2CH_3)_4]_2[Hg(OTeF_5)_4]$, $[N(CH_3)_4]_3[Hg(OTeF_5)_5]$, $[N(CH_2CH_3)_4]_3[Hg(OTeF_5)_5]$, $[N(CH_3)_4]_2[Hg_2(OTeF_5)_6]$, $Cs_2[Hg(OTeF_5)_4]\cdot Hg(OTeF_5)_2$, and $\{Cs_3[Hg_2(OTeF_5)_7]\cdot Hg(OTeF_5)_2\}\cdot 4SO_2ClF$. This material is available free of charge via the Internet at http://pubs.acs.org.

■ AUTHOR INFORMATION

Corresponding Author

*E-mail: schrobil@mcmaster.ca.

Notes

The authors declare no competing financial interest.

■ ACKNOWLEDGMENTS

We thank the Natural Sciences and Engineering Research Council of Canada for support in the form of a Discovery Grant (G.J.S.) and graduate scholarship (J.R.D.), Ontario Ministry of Training, Colleges, and Universities for a graduate scholarship (J.R.D.), and SHARCNet (Shared Hierarchical Academic

DOI: 10.1021/ic502602p
Inorg. Chem. 2015, 54, 1606−1626

Research Computing Network, www.sharcnet.ca) for providing the computational resources. We also thank J. P. Paxon for preliminary work on $Cs_2[Hg(OTeF_5)_4]\cdot Hg(OTeF_5)_2$.

REFERENCES

(1) House, D. A.; Robinson, W. T.; McKee, V. *Coord. Chem. Rev.* **1994**, *135/136*, 533−586.
(2) Svensson, P. H.; Kloo, L. *Inorg. Chem.* **1999**, *38*, 3390−3393.
(3) Pabst, I.; Bats, J. W.; Fuess, H. *Acta Crystallogr.* **1990**, *B46*, 503−508.
(4) Pickardt, J.; Wischlinsky, P. *Z. Anorg. Allg. Chem.* **1996**, *622*, 1125−1128.
(5) Clegg, W.; Greenhalgh, D. A.; Straughan, B. P. *J. Chem. Soc., Dalton Trans.* **1975**, *23*, 2591−2593.
(6) Sharma, R. P.; Sharma, R.; Kumar, A.; Venugopalan, P.; Brando, P.; Felix, V. *Inorg. Chem. Commun.* **2009**, *12*, 945−947.
(7) Battaglia, L. P.; Corradi, A. B. *J. Chem. Soc., Dalton Trans.* **1986**, *12*, 2529−2533.
(8) Brodersen, K.; Thiele, G.; Görz, G. *Z. Anorg. Allg. Chem.* **1973**, *401*, 217−314.
(9) Berthold, H. J.; Haas, D.; Tamme, R.; Brodersen, K.; Jensen; Kesser, D.; Thiele, G. *Z. Anorg. Allg. Chem.* **1979**, *456*, 29−40.
(10) Loukil, M.; Kabadou, A.; Svoboda, I. *J. Chem. Crystallogr.* **2008**, *38*, 85−9.
(11) Pickardt, J.; Wischlinski, P. *Z. Anorg. Allg. Chem.* **1999**, *625*, 1527−1531.
(12) House, D. A.; McKee, V.; Robinson, W. T. *Inorg. Chim. Acta* **1989**, *160*, 71−76.
(13) Pickardt, J.; Kuhn, B. *J. Chem. Soc., Chem. Commun.* **1995**, *4*, 451−452.
(14) Hoppe, R.; Homann, R. *Z. Anorg. Allg. Chem.* **1969**, *369*, 212−216.
(15) Schrötter, F.; Müller, B. G. *Z. Anorg. Allg. Chem.* **1992**, *618*, 53−58.
(16) Riedel, S.; Kaupp, M.; Pyykkö, P. *Inorg. Chem.* **2008**, *47*, 3379−3383.
(17) Sladky, F.; Kropshofer, H. *Inorg. Nucl. Chem. Lett.* **1972**, *8*, 195−197.
(18) Birchall, T.; Myers, R. D.; de Waard, H.; Schrobilgen, G. J. *Inorg. Chem.* **1982**, *21*, 1068−1073.
(19) Kellett, P. J.; Pawlik, M. J.; Taylor, L. F.; Thompson, R. G.; Levstik, M. A.; Anderson, O. P.; Strauss, S. H. *Inorg. Chem.* **1989**, *28*, 440−441.
(20) Strauss, S. H.; Noirot, M. D.; Anderson, O. P. *Inorg. Chem.* **1986**, *25*, 3850−3851.
(21) Huppmann, P.; Hartl, H.; Seppelt, K. *Z. Anorg. Allg. Chem.* **1985**, *524*, 26−32.
(22) Strauss, S. H.; Noirot, M. D.; Anderson, O. P. *Inorg. Chem.* **1985**, *24*, 4307−4311.
(23) Colsman, M. R.; Noirot, M. D.; Miller, M. M.; Anderson, O. P.; Strauss, S. H. *J. Am. Chem. Soc.* **1988**, *110*, 6886−6888.
(24) Rack, J. J.; Hurlburt, P. K.; Kellett, P. J.; Luck, J. S.; Anderson, O. P.; Strauss, S. H. *Inorg. Chim. Acta* **1996**, *242*, 71−79.
(25) Hurlburt, P. K.; Anderson, O. P.; Strauss, S. H. *J. Am. Chem. Soc.* **1991**, *113*, 6277−6278.
(26) Newbound, T. D.; Colsman, M. R.; Miller, M. M.; Wulfsberg, G. P.; Anderson, O. P.; Strauss, S. H. *J. Am. Chem. Soc.* **1989**, *111*, 3762−3764.
(27) DeBackere, J. R.; Mercier, H. P. A.; Schrobilgen, G. J. *J. Am. Chem. Soc.* **2014**, *136*, 3888−3903.
(28) Mercier, H. P. A.; Moran, M. D.; Schrobilgen, G. J.; Steinberg, C.; Suontamo, R. J. *J. Am. Chem. Soc.* **2004**, *126*, 5533−5548.
(29) Noirot, M. D.; Anderson, O. P.; Strauss, S. H. *Inorg. Chem.* **1987**, *26*, 2216−2223.
(30) Moran, M. D.; Mercier, H. P. A.; Schrobilgen, G. J. *Inorg. Chem.* **2007**, *46*, 5034−5045.
(31) Turowsky, L.; Seppelt, K. *Z. Anorg. Allg. Chem.* **1991**, *602*, 79−87.
(32) Mercier, H. P. A.; Sanders, J. C. P.; Schrobilgen, G. J. *Inorg. Chem.* **1995**, *34*, 5261−5273.
(33) Mercier, H. P. A.; Sanders, J. C. P.; Schrobilgen, G. J. *J. Am. Chem. Soc.* **1994**, *116*, 2921−2937.
(34) Van Seggen, D. M.; Hurlburt, P. K.; Anderson, O. P.; Strauss, S. H. *Inorg. Chem.* **1995**, *34*, 3453−3464.
(35) Hurlburt, P. K.; Rack, J. J.; Dec, S. F.; Anderson, O. P.; Strauss, S. H. *Inorg. Chem.* **1993**, *32*, 373−374.
(36) Hurlburt, P. K. Ph.D. Thesis, Colorado State University, Fort Collins, CO, 1993.
(37) Gerken, M.; Hazendonk, P.; Iuga, A.; Mack, J. P.; Mercier, H. P. A.; Schrobilgen, G. J. *J. Fluorine Chem.* **2006**, *127*, 1328−1338.
(38) Ivanova, M. V.; Köchner, T.; Mercier, H. P. A.; Schrobilgen, G. J. *Inorg. Chem.* **2013**, *52*, 6806−6819.
(39) Einstein, F. W. B.; Jones, R. D. G. *J. Chem. Soc. A* **1971**, 2762−2766.
(40) Casey, C. P.; Meszaros, M. W.; Neumann, S.; Genick Cesa, I.; Haller, K. J. *Organomet.* **1985**, *4*, 143−149.
(41) Mercier, H. P. A.; Moran, M. D.; Sanders, J. C. P.; Schrobilgen, G. J. *Inorg. Chem.* **2005**, *44*, 49−60.
(42) Bondi, A. *J. Phys. Chem.* **1964**, *68*, 441−451.
(43) Pauling, L. *The Nature of the Chemical Bond*, 3rd ed.; Cornell University: Ithaca, NY, 1960; p 260.
(44) Colsman, M. R.; Newbound, T. D.; Marshall, L. J.; Noirot, M. D.; Miller, M. M.; Wulfsberg, G. P.; Frye, J. S.; Anderson, O. P.; Strauss, S. H. **1990**, *112*, 2349−2362.
(45) Gillespie, R. J.; Hargittai, I. In *The VSEPR Model of Molecular Geometry*; Allyn and Bacon: Boston, MA, 1991; pp 127−130.
(46) Addison, A. W.; Rao, T. N. *J. Chem. Soc., Dalton Trans.* **1984**, *7*, 1349−1356.
(47) Kabisch, G. *J. Raman Spectrosc.* **1980**, *9*, 279−285.
(48) Herstedt, M.; Henderson, W. A.; Smirnov, M.; Ducasse, L.; Servant, L.; Talaga, D.; Lassègues, J. C. *J. Mol. Struct.* **2006**, *783*, 145−156.
(49) Glaucio, B.; Ferreira, G. B.; Comerlato, N. M.; Wardell, J. L.; Hollauer, E. *J. Braz. Chem. Soc.* **2004**, *15*, 951−963.
(50) *NBO 6.0.*; Glendening, E. D.; Badenhoop, J. K.; Reed, A. E.; Carpenter, J. E.; Bohmann, J. A.; Morales, C. M.; Landis, C. R.; Weinhold, F. Theoretical Chemistry Institute, University of Wisconsin, Madison, WI, 2013.
(51) Casteel, W. J., Jr.; Dixon, D. A.; Mercier, H. P. A.; Schrobilgen, G. J. *Inorg. Chem.* **1996**, *35*, 4310−4322.
(52) Sladky, F.; Kropshofer, H.; Leitzke, O.; Peringer, P. *J. Inorg. Nucl. Chem.* **1976**, *H. H. Hyman Memorial Volume*, 69−71.
(53) Mercier, H. P. A.; Sanders, J. C. P.; Schrobilgen, G. J. *J. Am. Chem. Soc.* **1994**, *116*, 2921−2937.
(54) Moock, K.; Seppelt, K. *Z. Anorg. Allg. Chem.* **1988**, *561*, 132−138.
(55) Schack, C.; Wilson, R. D. *Inorg. Chem.* **1970**, *9*, 311−314.
(56) Gerken, M.; Dixon, D. A.; Schrobilgen, G. J. *Inorg. Chem.* **2000**, *39*, 4244−4255.
(57) APEX2, release v2011.6−1; Bruker AXS, Inc.: Madison, WI, 1995.
(58) Sheldrick, G. M. *SADABS (Siemens Area Detector Absorption Corrections)*, version 2.03; Madison, WI, 1999.
(59) Sheldrick, G. M. *SHELXTL-Plus*, release 5.1; Siemens Analytical X-ray Instruments, Inc.: Madison, WI, 1998.
(60) Spek, A. L. *J. Appl. Crystallogr.* **2003**, *36*, 7−13.
(61) Weigend, F.; Ahlrichs, R. *Phys. Chem. Chem. Phys.* **2005**, *7*, 3297−3305.
(62) Peterson, K. A.; Figgen, D.; Goll, E.; Stoll, H.; Dolg, M. *J. Chem. Phys.* **2003**, *119*, 11113−11123.
(63) Andrae, D.; Haeussermann, U.; Dolg, M.; Stoll, H.; Preuss, H. *Theor. Chim. Acta* **1990**, *77*, 123−141.
(64) Basis sets and pseudo-potentials were obtained from the Extensible Computational Chemistry Environment Basis set Database, version 2/25/04, as developed and distributed by the Molecular Science Computing Facility, Environmental and Molecular Science Laboratory, which is part of the Pacific Northwest Laboratory, P.O. Box 999, Richland, WA 99352.

DOI: 10.1021/ic502602p
Inorg. Chem. 2015, 54, 1606−1626

(65) Frisch, M. J.; Trucks, G. W.; Schlegel, H. B.; Scuseria, G. E.; Robb, M. A.; Cheeseman, J. R.; Scalmani, G.; Barone, V.; Mennucci, B.; Petersson, G. A.; Nakatsuji, H.; Caricato, M.; Li, X.; Hratchian, H. P.; Izmaylov, A. F.; Bloino, J.; Zheng, G.; Sonnenberg, J. L.; Hada, M.; Ehara, M.; Toyota, K.; Fukuda, R.; Hasegawa, J.; Ishida, M.; Nakajima, T.; Honda, Y.; Kitao, O.; Nakai, H.; Vreven, T.; Montgomery, J. A., Jr.; Peralta, P. E.; Ogliaro, F.; Bearpark, M.; Heyd, J. J.; Brothers, E.; Kudin, K. N.; Staroverov, V. N.; Kobayashi, R.; Normand, J.; Raghavachari, K.; Rendell, A.; Burant, J. C.; Iyengar, S. S.; Tomasi, J.; Cossi, M.; Rega, N.; Millam, N. J.; Klene, M.; Knox, J. E.; Cross, J. B.; Bakken, V.; Adamo, C.; Jaramillo, J.; Gomperts, R.; Stratmann, R. E.; Yazyev, O.; Austin, A. J.; Cammi, R.; Pomelli, C.; Ochterski, J. W.; Martin, R. L.; Morokuma, K.; Zakrzewski, V. G.; Voth, G. A.; Salvador, P.; Dannenberg, J. J.; Dapprich, S.; Daniels, A. D.; Farkas, Ö.; Ortiz, J. V.; Cioslowski, J.; Fox, D. J. *Gaussian 09*, revision D.01 ; Gaussian, Inc.: Wallingford, CT, 2009.
(66) *GaussView*, release 3.0; Gaussian, Inc.: Pittsburgh, PA, 2003.

DOI: 10.1021/ic502602p
Inorg. Chem. 2015, 54, 1606−1626